

**MULTISCALE COMPUTATIONAL MODELING OF ROS-
GENERATING CHEMOTHERAPIES IN HEAD AND NECK
SQUAMOUS CELL CARCINOMA**

A Dissertation

Presented to

The Academic Faculty

by

Andrew Raddatz

In Partial Fulfillment

of the Requirements for the Degree

Doctor of Philosophy in the

Wallace H. Coulter Department of Biomedical Engineering

Georgia Institute of Technology and Emory University

May 2023

COPYRIGHT 2023 BY ANDREW RADDATZ

**MULTISCALE COMPUTATIONAL MODELING OF ROS-
GENERATING CHEMOTHERAPIES IN HEAD AND NECK
SQUAMOUS CELL CARCINOMA**

Approved by:

Dr. Melissa Kemp, Advisor

Wallace H. Coulter Department of
Biomedical Engineering

Georgia Institute of Technology

Emory University

Dr. Peng Qiu

Wallace H. Coulter Department of
Biomedical Engineering

Georgia Institute of Technology

Emory University

Dr. Cristina Furdui

Department of Internal Medicine, Section
on Molecular Medicine

Wake Forest School of Medicine

Dr. Susan Thomas

George W. Woodruff School of
Mechanical Engineering

Georgia Institute of Technology

Dr. Eberhard Voit

Wallace H. Coulter Department of
Biomedical Engineering

Georgia Institute of Technology

Emory University

Date Approved: April 5, 2023

ACKNOWLEDGEMENTS

I want to thank my PhD advisor Melissa Kemp for encouraging me and providing incredible inspiration to try new things and pursue my own ideas. However, I can get extremely excited about new ideas and sometimes have a hard time following through finishing projects. I am grateful for her grace with me as I developed the skills to conclude projects.

I also want to thank the entire Kemp Lab past and present for helping me with every aspect of my thesis work. They are supportive and provide brilliant minds with which to flesh out any and all research ideas.

Finally, I would especially like to thank my parents Robin and Dave Raddatz and my brothers Michael and Christopher Raddatz. My parents would always encourage me when I doubted myself. My brothers gave me calm and collected advice even when I was extremely stressed. Their critical thinking, dedication, care, and ability to pursue their passions are qualities I hope to emulate as I move into the next stage of my career.

TABLE OF CONTENTS

ACKNOWLEDGEMENTS	iii
LIST OF TABLES	vii
SUMMARY	X
CHAPTER 1 INTRODUCTION.....	1
1.1 Specific Aims	2
1.1.1 Aim 1. Quantify the importance of redox regulatory enzymes on ROS- generating chemotherapeutics in HNSCC.....	2
1.1.2 Aim 2a. Characterize the relationship between spatial information and antioxidant expression in HNSCC spheroids	2
1.1.3 Aim 2b. Engineer an agent-based model to simulate the generation, transport, and degradation of H₂O₂ in HNSCC treated with ROS-generating chemotherapeutics	2
CHAPTER 2 BACKGROUND	3
2.1 Head and Neck Squamous Cell Carcinoma.....	3
2.1.1 Epidemiology	3
2.1.2 Hypoxia and Redox Biology of HNSCC.....	4
2.1.3 Current HNSCC Treatment Options.....	5
2.2 NQO1-Bioactivatable Chemotherapeutics	6
2.3 Three-Dimensional <i>in vitro</i> Cancer Models.....	8
2.3.1 Effects on Oxygen Metabolism	9
2.4 Computational Modeling of Cancer.....	10
2.4.1 Differential Equation-Based Chemotherapeutic Models	11
2.4.2 Agent-Based Models of Cancer Growth and Treatment.....	12
CHAPTER 3 SINGLE CELL KINETIC MODELING OF β-LAPACHONE METABOLISM IN HEAD AND NECK SQUAMOUS CELL CARCINOMA	14
3.1 Introduction.....	14
3.2 Materials and Methods.....	15
3.2.1 Ordinary Differential Equation Model Construction	15
3.2.2 Sensitivity Analysis	17
3.2.3 Single Cell RNA Sequencing Data Analysis	17
3.3 Results	18
3.3.1 A Systems Level Model of ROS Generation by Quinone Cycling.....	18

3.3.2 Head and neck squamous cell carcinoma cells exhibit heterogeneity of redox gene expression.....	19
3.3.3 Initializing single cell ODE models with scRNA-seq	22
3.3.4 Sensitivity analysis shows H ₂ O ₂ production is insensitive to individual enzymatic parameters	23
3.3.5 Comparison of H ₂ O ₂ accumulation in healthy and cancer cells identifies patients with greatest potential for targeted therapy	25
3.3.6 Initializing single cell ODE models with patient HNSCC scRNA-seq identifies proteins most correlated with H ₂ O ₂ production	27
3.4 Discussion.....	29
CHAPTER 4 EXPERIMENTAL QUANTIFICATION OF PERTURBATION EFFECTS ON β-LAPACHONE METABOLISM IN HEAD AND NECK SQUAMOUS CELL CARCINOMA.....	35
4.1 Introduction.....	35
4.2 Materials and Methods.....	35
4.2.1 Cell Lines and Culture.....	35
4.2.2 siRNA Transfection	36
4.2.3 Amplex Red Measurements	36
4.3 Results	37
4.3.1 Co-culture of NQO1 knockdown and wildtype cells shows dependence of H ₂ O ₂ buildup on NQO1 expression.....	37
4.3.2 Experimental knockdown of NQO1 shows changes in levels of NQO1, Nrf2, and PRDX1.	38
4.3.3 Experimental knockdown of antioxidant enzymes shows lack of effect on H ₂ O ₂ buildup.	39
4.4 Discussion.....	42
CHAPTER 5 THE ROLE OF TUMOR ARCHITECTURE AND HETEROGENEOUS ANTIOXIDANT EXPRESSION ON β-LAPACHONE DRUG POTENCY	44
5.1 Introduction.....	44
5.2 Materials and Methods.....	47
5.2.1 Cell Lines and Culture.....	47
5.2.2 Generation and processing of spheroids to provide fluorescence microscopy samples.....	47
5.2.3 Immunofluorescence microscopy	48

5.2.4	Processing of microscopy images to collect single cell data	49
5.2.5	Analysis of spatial single cell data	50
5.2.6	Extracellular concentration grids and diffusion	51
5.2.7	Cell death mechanism.....	52
5.2.8	Simplified ABM.....	52
5.2.9	Intracellular ODE model.....	53
5.2.10	Intracellular ODE parameterization.....	54
5.3	Results	55
5.3.1	Logic of agent-based models	55
5.3.2	Simple agent-based model highlights architectural effects on H ₂ O ₂ production and cell death.....	57
5.3.3	Mixed tumorsphere imaging and quantified protein expression analysis.....	58
5.3.4	Parameterization of complex agent-based model	61
5.3.5	Complex ABM analysis	61
5.4	Discussion.....	63
CHAPTER 6 CONCLUSIONS AND FUTURE WORK		68
6.1	Conclusions.....	68
6.2	Future Work.....	70
6.2.1	Expansion of intracellular ODE model.....	70
6.2.2	Characterization and modeling of patient tumor samples.....	71
6.2.3	Improved <i>in vitro</i> 3D models.....	72
6.3	Summary.....	72
APPENDIX		74
A.1.	Chapter 3 Appendix.....	74
A.2.	Chapter 5 Appendix.....	78
REFERENCES.....		79

LIST OF TABLES

Table 1: Additional rate terms for ODE model	16
Table 2: ODEs included in ABM intracellular model	54
Table 4: Parameter Adjustments	74
Table 5: Initial Species Adjustments.....	76

LIST OF FIGURES

Figure 1: Generation of a relevant model of drug metabolism and hydrogen peroxide clearance pathways.	19
Figure 2: Head and neck cancers demonstrate intratumor and intertumor redox heterogeneity.	21
Figure 3: Sensitivity analyses.....	24
Figure 4: Model results using single cell gene expression values.....	26
Figure 5: Partial least squares regression VIP scores and loadings.....	28
Figure 6: H ₂ O ₂ buildup over time during β -lapachone treatment based on amount of NQO1 ⁺ cells.	37
Figure 7: NQO1 expression levels after siRNA knockdown.	39
Figure 8: siRNA perturbation studies validate sensitivity analyses.	41
Figure 9: Agent-based model for β -lapachone metabolism.	56
Figure 10: Simple ABM results show impact of architecture and death threshold on cell type viability.....	58
Figure 11: Cyclic immunofluorescence and single cell expression quantification.	61
Figure 12: Complex ABM viability results show viability dependence on rSCC percentage.	62
Figure 13: Correlations between protein intensity and distance from center of tumorsphere.	78

LIST OF SYMBOLS AND ABBREVIATIONS

ABM	Agent-based model
ARE	Antioxidant response element
HIF-1 α	Hypoxia-inducible factor 1-alpha
HNSCC	Head and neck squamous cell carcinoma
HPV	Human papillomavirus
IB-DNQ	Isobutyl deoxyxyboquinone
NADPH	Nicotinamide adenine dinucleotide phosphate
NQO1	NAD(P)H quinone dehydrogenase 1
Nrf2	Nuclear factor-erythroid factor 2-related factor 2
ODE	Ordinary differential equation
PARP1	poly(ADP-ribose)polymerase 1
PPP	Pentose phosphate pathway
ROS	Reactive oxygen species
scRNA-seq	Single cell RNA sequencing

SUMMARY

Unlike promising developments for many cancers in the past decade, head and neck cancer has not realized the gains in 5-year survivability nor approval of many new therapeutic strategies. New computational and experimental techniques are crucial to better understand the disease. The cancer scientific community has recently begun to understand the role of tumor heterogeneity in the complexity of both cancer biology and how these cancers respond to treatment. Additionally, computational tools to simulate drug mechanism of action and cell-cell communication that occurs during treatment has been shown to provide important insights that experimentalists can then utilize when developing treatments and how best to apply them.

To expand the community's knowledge of head and neck cancer in response to chemotherapeutic treatment and the impact that tumor heterogeneity plays in this process, I developed a dynamic intracellular drug metabolism model and a microscopy-based pipeline to analyze and simulate the impact of tumor heterogeneity on drug response. In the dynamic intracellular drug metabolism model, I focused on ROS-generating chemotherapies, specifically β -lapachone, and the reduction of these ROS by constructing an ordinary differential equation system representing the enzymatic reactions of drug metabolism and ROS reduction on a single cell level. I compared patients' healthy and cancer cells by their simulated production rates of ROS during β -lapachone treatment and found that treatment could be cancer-targeting depending on the patient and the enzyme profiles of their cells. Furthermore, the output features of these simulations in machine learning algorithms identified which combinations of enzymes were most important to the model, providing potential biomarkers to be probed for when applying these drugs to animal or human studies.

In order to probe how spatial distribution of heterogeneous redox enzymes could impact β -lapachone potency non-uniformly within tumors, I developed an agent-based model that accounts for diffusion for drug metabolized H_2O_2 to simulate how neighboring cells interact with one another under treatment. The developed agent-based model uses experimentally-determined location and expression values of enzymes as input to predict oxygen and ROS concentration profiles as well as cell viability at various time points. The model demonstrates that spatial tumor heterogeneity impacted drug potency depending on the expression of the antioxidant enzymes and location within a tumor, reflecting known bystander effect of β -lapachone. Agent-based simulations suggest that the more heterogeneous a tumor is, the more effective β -lapachone will be due to an increased bystander effect given similar bulk phenotypes.

CHAPTER 1 INTRODUCTION

Head and neck squamous cell carcinoma (HNSCC) affects approximately 50,000 new people each year. Many HNSCC tumors resist standard chemotherapies and radiation treatment due to the upregulation of nuclear factor-erythroid factor 2-related factor 2 (Nrf2), a transcription factor that controls cellular reactive oxygen species (ROS) levels through transcriptional control over antioxidant enzymes such as catalase, peroxiredoxin, and NADPH quinone oxidoreductase 1 (NQO1). A potential method of treatment is to use NQO1-activatable chemotherapeutic agents, such as β -lapachone and isobutyl-deoxyxyboquinone (IB-DNQ), which produce ROS leading to cell death through programmed necrosis. The efficacy of these chemotherapeutics for solid tumors is still under investigation, and currently patient-specific metrics of response have not been identified. HNSCC is a highly heterogeneous cancer, including expression of NQO1 which metabolizes the drug. In other cancers, tumor heterogeneity can be leveraged for the “bystander effect”; cells that are not directly affected by the drug can be damaged or killed by apoptosis due to the metabolism of the drug in a nearby cell. Even though redox-associated proteins are well characterized in their individual mechanisms, a more thorough approach to elucidate their quantitative significance on a systems level both intracellularly and on the broader tissue scale is necessary for this drug to be effectively utilized in the clinical setting.

Ultimately, the **objective** of this project as executed in the following aims will relate antioxidant expression and ROS-generating chemotherapy efficacy, and utilize this knowledge to engineer personalized, computational models of HNSCC in response to ROS-generating chemotherapies.

1.1 Specific Aims

1.1.1 Aim 1. Quantify the importance of redox regulatory enzymes on ROS-generating chemotherapeutics in HNSCC

I *hypothesized* that the efficacy of ROS-generating drugs is dependent on a balance of antioxidant enzymes. A mechanistic ODE model implemented with single cell resolution representing production and scavenging of H_2O_2 was developed and parameterized using transcriptomic (single cell RNAseq) and proteomic data. Experimental perturbations tested model predictions of systems behavior of quinone-based futile cycling and cell-line specific cytotoxicity.

1.1.2 Aim 2a. Characterize the relationship between spatial information and antioxidant expression in HNSCC spheroids

I *hypothesized* that intratumor hypoxia results in varied oxygen levels and altered antioxidant enzyme expression which can be related to each other spatially. In this aim, engineered HNSCC spheroids were used to investigate the regulation of antioxidant enzyme expression due to 3D *in vitro* culture systems of defined heterogeneity.

1.1.3 Aim 2b. Engineer an agent-based model to simulate the generation, transport, and degradation of H_2O_2 in HNSCC treated with ROS-generating chemotherapeutics

I *hypothesized* that personalized models of antioxidant systems can be used to improve treatment outcome predictions. In this aim, the ODE model developed in Aim 1 was simplified and integrated with an agent-based model to simulate the redox environment within HNSCC tumors undergoing β -lapachone treatment. The model simulated the effectiveness of β -lapachone treatment in HNSCC tumor spheroids by using cyclic immunofluorescence images to initialize cell networks.

CHAPTER 2 BACKGROUND

2.1 Head and Neck Squamous Cell Carcinoma

2.1.1 Epidemiology

2022 is expected to have more than 50,000 cases of head and neck cancer in the United States with 10,000 deaths resulting from the disease (1). HNSCC is anatomically diverse, arising from epithelial cells on mucosal linings within the head and neck region including the oral cavity, pharynx, larynx, paranasal sinuses, and salivary glands (2). HNSCC is classified as human papillomavirus (HPV)-positive or HPV-negative, with the main risk factors for HPV-negative HNSCC being smoking and drinking alcohol (3–5). While HPV-negative incidences are decreasing due to increasing awareness of the dangers of smoking and drinking, the response and survival rates for HPV-negative tumors remains significantly lower than HPV-positive tumors (6–8). HPV-positive HNSCC is typically a more radiosensitive tumor making HPV-negative HNSCC more challenging to treat (9). An additional potential disadvantage of HPV-negative HNSCC is that this type of cancer has a lower immune response than HPV-positive HNSCC shown by higher levels of immune cell infiltration (10,11).

Heterogeneous HNSCC can lead to worse outcomes than more uniform tumors. A study that analyzed publicly available sequencing data on 74 patients with HNSCC showed that the patients with poor outcome had high genetic heterogeneity when using the mutant-allele tumor heterogeneity (MATH) metric (12). The relationship between the MATH score and outcome was actually stronger than other poor-outcome HNSCC biomarkers such as HPV status or the tumor protein p53 tumor suppressor gene. Another study investigating the heterogeneity of HNSCC comparing differences between cell lines and

tumors found sets of genes that were only mutated in cell lines and others that were only mutated in tumors, but concluded with a set of overlapping mutated genes between tumors and cell lines that they suggested should be the focus on preclinical trials (13).

2.1.2 Hypoxia and Redox Biology of HNSCC

Due to disorganized vasculature and rapid proliferation, regions within solid tumors including HNSCC can experience hypoxia where the oxygen tension is low (14–18). A wide variety of cell phenotypes within a tumor can result based on the local availability of oxygen per cell. Cells in extremely low oxygen environments will be incapable of metabolizing glucose efficiently via oxidative metabolism; in regions where ATP production is insufficient the cells undergo cell death leading to what is known as a necrotic core. Tumor hypoxia has been reported to be a clinical indicator of poor prognosis (19,20). Hypoxia is associated with ROS production because mitochondrially-produced ROS activate HIF-1 α , a main hypoxia-related transcription factor (21). In the mitochondria, Complex III produces ROS under normoxia, and in hypoxic conditions the production of ROS increases which leads to a stabilization of the HIF-1 α protein (22).

In both healthy and cancerous cells, ROS are managed by antioxidant enzymes which are upregulated via the Nrf2-Keap1 pathway. Without ROS, Nrf2 remains bound to Keap1 which tags it for ubiquitination and subsequent degradation (23). Under oxidative stress due to ROS, Keap-1 is oxidized and unbinds to Nrf2 allowing it to translocate to the nucleus. Many enzymes are regulated by the Nrf2 transcription factor, and they can be categorized as proteins which have genes that contain an antioxidant response element (ARE). Elevated ROS levels are frequently elevated in tumors and associated with downstream tumor-promoting outcomes (24). Moderate levels of ROS are tumor

promoting because they increase proliferation, initiate angiogenesis, and trigger survival signaling pathways; however, if ROS levels are elevated even further, the cancer cells will undergo cell death or senescence (24–28). Cancer cells do not have to experience as much of an increase in ROS levels as healthy cells to die, which is the rationale behind using ROS-generating chemotherapies such as β -lapachone, isobutyl-deoxynyboquinone, and elesclomol (29–32). Drugs that can elevate ROS levels from tumor-promoting to tumor-inhibiting can lead to cancer cell death while normal healthy cells are only pushed into the tumor-promoting ROS level regime for a brief amount of time.

2.1.3 Current HNSCC Treatment Options

In 2022, many different clinical options exist to treat HNSCC. Traditionally, chemotherapy and/or radiation have served as the means to treat head and neck squamous cell carcinoma after surgical resection of the primary tumor, but if the tumor is located in the pharynx or larynx, radiation without surgery is more common with moderate accelerated radiotherapy performing better than conventional fractionated radiotherapy of the same dose in laryngeal cancer, indicated by a hazard ratio of loco-regional failure of 0.72 (33,34). A potential complication that must be taken into account is preservation of function of the mouth and throat when utilizing surgery, but improved surgical techniques that are less invasive have made this less of a concern (35). If pathological features indicate increased risk of recurrence, high-dose cisplatin with radiation can improve disease-free survival compared to if only radiation is used with a hazard ratio of 0.75 and overall 5-year survival Kaplan-Meier estimates improving from 40 to 53 percent, but using chemoradiotherapy after surgery can be very toxic so having a precise understanding of the severity of the disease is important (36). If the cancer is late stage and has spread to multiple

lymph nodes, only chemoradiotherapy is recommended since surgery will likely not remove enough of the tumor to make it worth removing function, and including chemotherapy in addition to radiation improves projected overall 5-year survival in these cases from 23 to 37 percent. Additionally, the EGFR inhibitor cetuximab has been shown to sensitize tumors to radiation in addition to platinum-based chemotherapy (37).

More recently, immunotherapy has been tested in HNSCC. Pembrolizumab, a PDL1 inhibitor, showed better outcomes in combination with a platinating agent and 5-fluorouracil than cetuximab with the same chemotherapy combination by improving overall survival from 10.7 months to 13 months (38). Many treatment regimens rely solely on the stage of the disease and how far it has progressed and do not take into account its phenotype, with immunotherapy targeting EGFR and PD-L1 being some of the first forays into treating these molecular phenotypes of HNSCC. Overall, there is a lot of room to improve treatment, and a large aspect of determining the proper treatment is not only properly diagnosing the disease stage, but also understanding its underlying biology which is on what this project focuses.

2.2 NQO1-Bioactivatable Chemotherapeutics

β -lapachone has been studied for decades and its antitumor properties have been investigated since the 80s. Originally understood to be a DNA topoisomerase I inhibitor and radiosensitizing agent (39), the mechanism of action involving futile redox cycling has become the focus of its studies more recently. Based on prior studies, β -lapachone is metabolized by NQO1, a Nrf2-regulated enzyme (40). This reaction reduces β -lapachone through the oxidation of NADPH converting the quinone to a hydroquinone. Following the

conversion, the hydroquinone then spontaneously reacts with molecular oxygen to revert to the quinone form through a semiquinone intermediate. This oxidation process causes the molecular oxygen to gain an electron resulting in the highly reactive species superoxide. Once the superoxide species has been generated, it can be dismutated into H_2O_2 with the addition of H_2 , a product which is also a destructive ROS with a longer half-life and diffusive pathlength (41). The intermediate superoxide is much more reactive and damaging; therefore conversion to H_2O_2 results in a ROS with multiple antioxidant pathways capable of mitigating oxidative stress within the cell. β -lapachone has proven successful in a number of different types of solid tumors and the mechanism has been confirmed multiple times by applying antioxidants and NQO1 inhibitors and seeing a reduction in drug efficacy (42–48). In 2007, Erik Bey et al. showed that non-small cell lung cancers expressing high levels of NQO1 were selectively killed by β -lapachone through the generation of ROS leading to hyperactivation of poly(ADP-ribose) polymerase 1 (PARP1), which led to further depletion of NAD^+ /ATP pools and apoptosis (43). Intratumoral delivery of β -lapachone in prostate cancer using polymer implants demonstrated that the low solubility of the drug could be overcome *in vivo* (48). In 2012, the drug's antitumor activity was shown to be killing through programmed necrosis due to the PARP1 hyperactivation (45).

Treatment with exogenous catalase to reduce the programmed necrosis was shown possible in NQO1-positive breast cancer in 2013, highlighting the role of ROS production in the antitumor mechanism since catalase reduces H_2O_2 to water (47). The supplementation of catalase to decrease the effectiveness of β -lapachone highlighted a need to focus on antioxidant enzyme expression levels in addition to NQO1, and subsequently

NQO1:catalase ratios for determining eligible cancers for the drug was introduced by Cao et al in 2014 (49). In the same study, the bystander effect was investigated by quantifying how cells with low NQO1:catalase ratios responded to β -lapachone treatment if they were in close proximity to cells with high NQO1:catalase ratios. DNA damage due to ROS production from β -lapachone was observed to be dependent on distance from cells with high NQO1 levels. In the following years, additional perturbations to antioxidant systems in cells were tested to see how they could improve β -lapachone sensitization. In 2015, targeting glutamine metabolism, which leads to production of both the important nonenzymatic antioxidant glutathione (GSH) and NADPH, resulted in increased sensitivity of pancreatic cancer to β -lapachone (44). Furthermore, in 2020 Torrente et al. demonstrated that targeting other antioxidant enzymes superoxide dismutase 1 (SOD1) and thioredoxin reductase 1 (TXNRD1) also improved performance of β -lapachone even in NSCLC cells with high Nrf2 expression that gave them β -lapachone resistance (50).

Based upon the molecular biology research that went into understanding how β -lapachone works and how its effectiveness can be affected by perturbing antioxidant systems in promising animal studies, two phase I clinical trials were conducted. The first began in 2012 in solid tumors and 42 patients with NQO1-high tumors were treated (51). At the end of the study with 32 of these patients evaluable, 12 responded with stable disease and 6 had tumor shrinkage. The conclusions of the study were that β -lapachone did not perform satisfactorily as a single agent.

2.3 Three-Dimensional *in vitro* Cancer Models

While *in vitro* studies are conducted most widely with cancer cell lines grown in colonies due to their convenience, the utility and accuracy of three-dimensional culture

systems is quickly becoming recognized. 3D cultures provide a more *in vivo* representative system by introducing physiological characteristics such as diffusion limitation and additional external mechanical cues, but they are typically less convenient than the standard 2D monolayer culture system (52–56). Functionally, the cells in 2D and 3D cancer systems differ in a number of ways including how they metabolize drugs, express genes and synthesize proteins, survive, and consume oxygen (57–61). Some of the most common methods for 3D culture systems include altering the cell culture media to promote spheroid formation (62), using agitation to suspend cells in a spinner flask (63), suspending cells in a hanging drop (64), using cell repulsive substrate coatings (65), and embedding cells in an extracellular matrix such as a hydrogel (66–68). Generally speaking, a 3D cancer model is one of the most accurate *in vitro* representations of an *in vivo* system (69,70), and their usage in the scientific community is becoming much more popular due to improving methods.

2.3.1 Effects on Oxygen Metabolism

Similar to how *in vivo* tumors have necrotic cores because of oxygen diffusion limitations, 3D *in vitro* culture systems result in a lack of oxygen in the center of the cultures. This spatial feature is a key difference between 2D and 3D *in vitro* models, because it allows for the investigation of how oxygen limitation can impact cell growth, cell phenotype, and the response to drug treatment. Typically, when cells are in an environment with less oxygen they tend to shift to a more glycolytic metabolism which does not require oxygen to generate ATP. An interesting phenomenon that occurs in cancers known as the Warburg effect leads to cancer cells having a more glycolytic phenotype even in the presence of oxygen (71). This effect can be explained by the fact

that cancer cells are rapidly dividing and require many resources to generate new daughter cells. Rather than breaking the glucose down entirely via oxidative phosphorylation into the maximum amount of ATP, the cell generates a minimal amount of ATP via glycolysis and utilizes the rest of the molecule to generate critical biomolecules via the pentose phosphate pathway (PPP). The PPP also generates NADPH which is a required redox cofactor in the enzymatic mechanism of NQO1. This phenomenon leads to a number of questions about the phenotype of cancer cells within both hypoxic and normoxic environments that are not obviously answered. Using a 3D culture system allows for a recapitulation of the spatial environment an *in vivo* tumor would have. With NQO1-activatable drugs, 3D culture systems are even more beneficial because these drugs require the presence of oxygen to complete their futile cycling and generate ROS; however, to date few studies investigating quinone cycling have leveraged this form of *in vitro* analysis.

2.4 Computational Modeling of Cancer

Computational models can provide great insight into real systems and drastically reduce required time and costs of research. While computational models are never a perfect representation of reality, they are used often to help understand a real system. Determining which variables in a real system are most important in a resultant outcome can be challenging, and computational models help to reduce the real system to its most crucial components. Once computational models are validated against experimental data, they can also be used to predict the outcome of situations that have conditions that are experimentally hard to generate in reality. While there is a plethora of types of

computational modeling tools, this section will focus on ordinary differential equation (ODE) models and agent-based models (ABMs) used for cancer.

2.4.1 Differential Equation-Based Chemotherapeutic Models

ODE models were originally used in oncology to understand tumor growth dynamics or carcinogenesis (72,73). Recently, ODE models of cancer signaling pathways and metabolism have increased in popularity due to the quickly accumulating molecular-based omics data (74–78). This form of modeling typically employs a mechanistic understanding of what is going on molecularly within their system of choice to develop their differential equation terms. Membrane permeation can be represented via Fick's law of diffusion. Enzymatic reactions can be represented via mass action where rates of reaction are determined by concentration of enzymes and reactants, or they can be represented by the more common Michaelis-Menten representation which includes a saturation term due to enzymes usually having relatively low concentration compared to the reactants. One method to simplify metabolic ODE models is to use parameter sensitivity analyses, as we have shown in the past in the context of redox systems and enzyme kinetics (79). There is typically a balance between comprehensively including every reaction related to the problem at hand and oversimplifying the model, so a sensitivity analysis can be done to rank the importance of each reaction based on how reactions and their associated parameters influence the outcome of interest. Some drawbacks include the fact that ODE models assume well-mixed compartments and there is a lack of spatial consideration which can limit the amount of knowledge to be gained.

2.4.2 Agent-Based Models of Cancer Growth and Treatment

ABMs on the other hand focus on the spatial variability within biological systems. ABMs consist of independent “agents” that take environmental cues to make decisions and allow for complex and emergent behaviors to occur such that a population of agents is more than just the sum of its parts. One of the first models that inspired ABMs was John Conway’s Game of Life which was a cellular automaton developed in 1970. With only four rules where spaces within the grid are only either “on” or “off”, the model is able to generate over a dozen patterns including “oscillators” and “spaceships”. ABMs expand upon this idea by creating more complex agents that can represent cells with more than one characteristic and set of rules. ABMs have been used to capture the complexity of cancer, such as the effects of hypoxia on cancer cell viability, angiogenesis, and migration to give rise to complex spatial organization (80–84). Over two decades ago, McDougall et al used simulated vasculature networks to understand how drug concentration would vary within a tumor context, motivating further investigations on the delivery of chemotherapeutic drugs (80). While this work demonstrated that distribution of chemotherapeutics is not uniform within a tumor, the authors did not investigate how this heterogeneous delivery would impact cell response. Work by Anderson et al. in 2009 looked at how oxygen limitations and consumption could impact cell states and growth patterns, finding that fingerlike projections of cells from the tumor can occur when cells are in poor nutrient microenvironments (82). More recently, Macklin et al have successfully developed a widely available ABM framework which has the capacity to include metabolism, diffusion within the microenvironment, sophisticated cell mechanics, and parallelization for improved computational efficiency of simulating large ($\sim 10^6$ cells) tumor systems (85).

Several examples of ABM software packages include Physicell (PhysiCell.MathCancer.org), NetLogo (ccl.northwestern.edu/netlogo), and CompuCell3D (www.compuCell3d.org). One area where questions still exist is concerning the phenomenon known as the bystander effect, where higher levels of drug-metabolizing cells can more effectively kill non-drug-metabolizing cells due to proximity and diffusion of drug metabolism byproducts. This has been explored with ABMs in the context of hypoxia-activated prodrugs using three dimensional cell cultures for validation, where the study found that modeling certain drugs such as PR104A in tumor spheroids lead to bystander effects while a drug like SN30000 does not due to their different pharmacology (86). Additionally, they found that penetration of the drug into the spheroids can be impeded leading to lower concentrations within the spheroid centers, but if the bystander effect and downstream metabolites of drug metabolism are produced at a high enough rate, this penetration problem is less of an issue. This ABM study showed how the bystander effect can be an important contribution to drug efficacy that can overcome spatial heterogeneity of a tumor either in the form of hypoxia or antioxidant expression.

CHAPTER 3 SINGLE CELL KINETIC MODELING OF β -LAPACHONE METABOLISM IN HEAD AND NECK SQUAMOUS CELL CARCINOMA

3.1 Introduction

Head and neck squamous cell carcinoma (HNSCC) is one of the most prevalent types of cancer globally (1). Prophylactic measures such as HPV vaccination and the reduction of alcohol consumption and smoking are improving outcomes; however, five-year survival rates of HPV-negative HNSCC remain lower than 60% (87). While the etiology of HNSCC and anatomical locations within the oral cavity epithelial tissue are diverse, a hallmark of this cancer is elevated oxidative stress (88). H_2O_2 at physiological concentrations is important as a second messenger for many signaling processes including the MAPK, PI3K, NF- κ B, and HIF pathways (89–93); however, H_2O_2 at higher levels promote tumorigenesis by causing genomic instability and proliferative signaling (94). If H_2O_2 levels are elevated even further, the level of oxidative stress cannot be managed and cells will go through one of several cell death mechanisms including necrosis, apoptosis, and ferroptosis (95,96). Cancer cells manage levels of H_2O_2 through multiple antioxidant enzyme systems (97), and under sustained oxidative stress will transcriptionally upregulate several antioxidant enzymes via the Keap1-Nrf2 axis (23,98). One treatment strategy is to selectively target cancer cells through the generation of H_2O_2 and disrupt the delicate balance these cells have between their higher antioxidant capacity and higher H_2O_2 levels (44,99–102). A unique approach to this strategy is utilizing NQO1-activatable quinone drugs to generate superoxide and H_2O_2 . NQO1 is an enzyme canonically involved in detoxifying reactive quinones by reducing them to their hydroquinone form, but NQO1-

activatable quinone drugs are oxidized back to their quinone form following NQO1 reduction, leading to a cycling of the drug and production of superoxide radicals. NQO1 is upregulated by Nrf2 (103), so this approach should selectively target cancer cells that have constitutive Nrf2 activation. Furthermore, it can be argued that the generation of acute superoxide and H_2O_2 by NQO1-activatable therapeutics can cause a positive feedback response leading to more NQO1 expression and enhanced lethality of these compounds, because high H_2O_2 levels activate nuclear translocation of Nrf2 (104). Numerous studies have shown the benefit of these types of drugs alone, and targeting additional antioxidant and survival systems concurrently can improve the efficacy of the drug (43,51,105,106); however, there is debate as to whether the currently considered metric of NQO1:catalase expression or activity ratio is useful for identifying tumors susceptible to NQO1-activatable quinone drugs (45,47,49,50). To improve our understanding of the complex interplay between various antioxidant systems and the production of superoxide and H_2O_2 by NQO1-activatable drugs, we developed and analyzed a differential equation model based on enzyme kinetic mechanisms that leverages the diversity of expression levels relevant to cancer redox systems. Furthermore, we explored potential uses for such a model by initializing parameter and species values using scRNA-seq data as a way to understand intratumor and patient variability in response to this type of chemotherapeutic intervention.

3.2 Materials and Methods

3.2.1 Ordinary Differential Equation Model Construction

The redox system ODE model was built upon a previously published model originally developed to describe the H_2O_2 clearance within Jurkat T cells in response to a

bolus of extracellular H_2O_2 addition (97). MATLAB R2020b was used and the ode system was solved with the ode15s solver with a max step of 1 second and an absolute tolerance of 10^{-8} . The additional species included in new reactions are: oxidized extracellular β -lapachone ($\beta\text{-lap}^{\text{ext}}$), intracellular $\text{O}_2^{\bullet-}$, oxidized intracellular β -lapachone ($\beta\text{-lapQ}$), reduced intracellular β -lapachone ($\beta\text{-lapHQ}$), semioxidized intracellular β -lapachone ($\beta\text{-lapSQ}$), and glutathionylated intracellular β -lapachone ($\beta\text{-lap-GSH}$). New reaction rate terms are provided in Table 1. Appendix Tables 3 and 4 list the complete range of parameters and initial values, respectively, derived from single cell transcriptomics and used within the ODE system which were updated from the model originally characterized for Jurkat cells (97).

Table 1: Additional rate terms for ODE model

Reaction Name	Rate Term
β -lap permeation*	$k_{34} * A^{\text{cells}} * ([\beta\text{-lap}^{\text{ext}}] - [\beta\text{-lapQ}])$
β -lap reduction	$k_{29} * [\beta\text{-lapQ}] * [\text{NADPH}]$
β -lap semioxidation	$k_{30} * [\beta\text{-lapHQ}] * [\text{O}_2]$
β -lap oxidation	$k_{31} * [\beta\text{-lapSQ}] * [\text{O}_2]$
superoxide dismutase	$k_{32} * [\text{O}_2^{\bullet-}]^2$
β -lap semireduction	$k_{33} * [\beta\text{-lapQ}] * [\text{NADPH}]$
β -lap glutathionylation	$k_{35} * [\beta\text{-lapHQ}] * [\text{GSH}]$
Glutathionylated β -lap permeation*	$k_{36} * A^{\text{cells}} * [\beta\text{-lapHQ-SG}]$

*Permeation rate terms are divided by respective compartment volumes

ODEs were solved with ode15s in MATLAB R2020b, using a max timestep of 1 second.

3.2.2 Sensitivity Analysis

Sensitivity values were calculated by increasing or decreasing parameter values by 10%, running the ODE solver for a simulated 2 hours, and using the following formula where $S_{i,j}$ represents the sensitivity of variable x_i to parameter k_j . If $S_{i,j}$ is negative it represents x_i changing in the opposite direction of the k_j .

$$S_{i,j}(t) = \frac{\partial x_i(t)/x_i(t)}{\partial k_j/k_j(t)} \quad (1)$$

3.2.3 Single Cell RNA Sequencing Data Analysis

HNSCC scRNA-seq data was collected from the gene expression omnibus (GEO Accession: GSE103322). This data had already been preprocessed to exclude cells with fewer than 2,000 genes detected or an average expression level below 2.5 of a curated list of housekeeping genes (107,108). The data set had also been clustered into malignant and non-malignant cells based on their expression of epithelial markers. Of the data from 18 patients, we retained the 10 patients' transcriptomes that contained the most cells classified as malignant cells as previously performed (107,109). t-SNE dimensional reduction was performed using the scikit-learn python library `scikit-learn.TSNE()` with 2 components and PCA initialization. Enzyme abundance calculations from scRNA-seq data was performed as previously described (110). Briefly, kinetic rate constants from a mechanistic model of RNA production, RNA degradation, protein production, and protein degradation were used to determine equilibrium protein abundances given RNA levels. 13 of the 14 protein values were derived using this mechanistic model and using the data in the original paper, these 13 predicted protein copy numbers correlate with the actual protein copy numbers with an R^2 of 0.933. For aquaporin 3 (AQP3) which facilitates H_2O_2 plasma membrane transport

and for which these rate constants were not given, linear regression between RNA and protein was used to estimate protein abundance. Partial least squares regression (PLSR) was performed with log-transformed and zero-mean unit variance standardized data in SIMCA 17 (Sartorius). Plots were generated using Seaborn and Matplotlib python libraries. The kernel density estimate plot was generated with default parameters using `seaborn.kdeplot()`. Scipy was used to conduct the Welch's t tests with `stats.ttest_ind()` and `equal_variance` set to `False`.

3.3 Results

3.3.1 A Systems Level Model of ROS Generation by Quinone Cycling

We developed our model system to encompass three main aspects: 1) sets of critical H₂O₂-stabilizing antioxidant systems; 2) metabolism of the xenobiotic drug β -lapachone; and 3) the permeation of key species across membranes of the cell, including organelle-specific transport. We assumed that mitochondrial H₂O₂ production would remain constant due to basal respiratory metabolism, and mitochondrial antioxidant systems were not included, nor did we factor in activation of NADPH oxidases as a source of superoxide as it has been shown that β -lapachone treatment does not alter NADPH oxidase activity leading to superoxide levels from NOXs remaining similar with or without treatment (111). Another assumption made was that due to high catalytic rates of NQO1 and antioxidant enzymes, 2 hours of simulated time was sufficient to capture the dynamics of the system. The relatively short period of simulated time allowed us to ignore transcriptional and translational regulation, such as how increased cellular oxidation would trigger Nrf2 nuclear translocation and upregulation of antioxidant genes including NQO1; therefore,

total enzyme concentrations were assumed constant. The system and directionality of reactions and transport are shown in Figure 1.

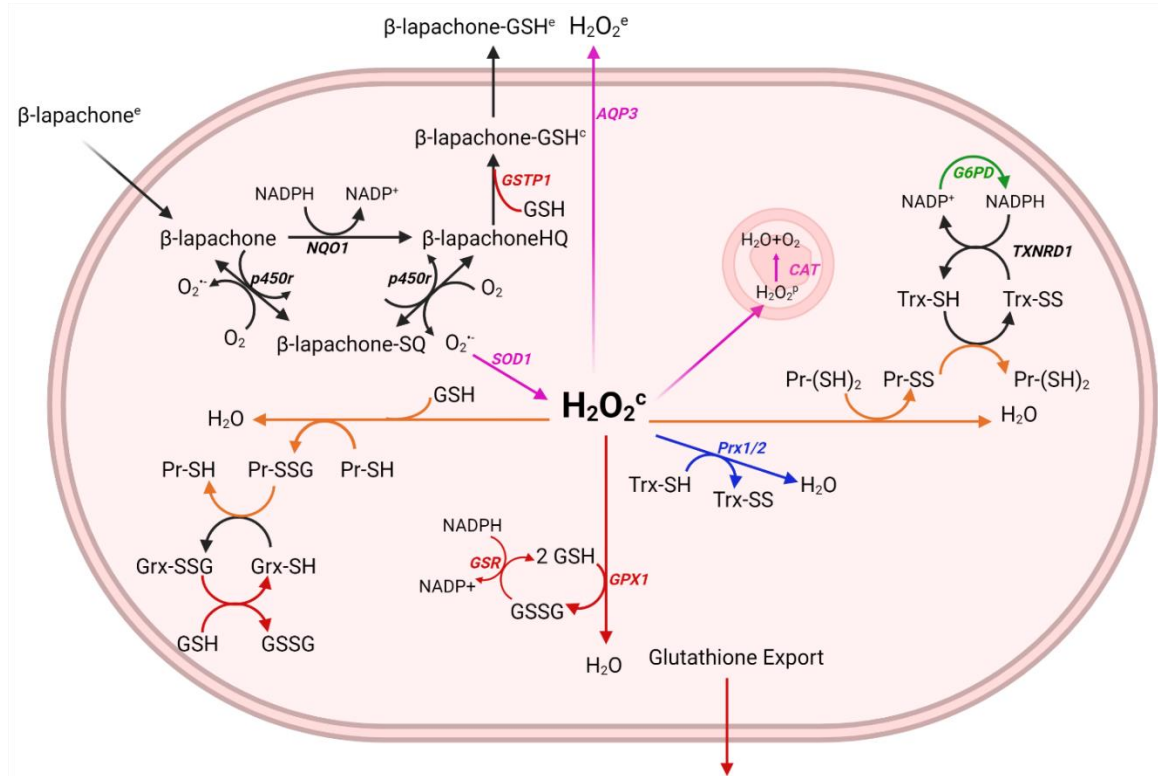


Figure 1: Generation of a relevant model of drug metabolism and hydrogen peroxide clearance pathways. The metabolism of β -lapachone by NQO1 results in the generation of superoxide ($O_2^{\cdot-}$) and the oxidation of NADPH. Superoxide dismutase 1 (SOD1) in the cytosol converts the superoxide to hydrogen peroxide (H_2O_2) which is converted to water and oxygen by antioxidant systems including the peroxiredoxin/thioredoxin/thioredoxin reductase/sulfiredoxin system, the glutathione peroxidase/glutathione/glutathione reductase system, catalase, and the oxidation of free protein thiols. NADPH often serves as the reductant for cycling these antioxidant enzymes and it is used to reduce β -lapachone, thus canonical metabolic reactions involved in the production of NADPH are also included, such as glucose-6-phosphate-dehydrogenase (G6PD).

3.3.2 Head and neck squamous cell carcinoma cells exhibit heterogeneity of redox gene expression

We sought to understand how variation in redox profiles of in vivo HNSCC tumors may reflect the distributed control of H_2O_2 clearance in tumor cells. To take advantage of

new highly resolved omics technologies that provide rich tumor characterization, we analyzed scRNA-seq data from 10 HNSCC patients originally collected by Puram et al (107). In this dataset, there is a varying degree of cell type representation from each patient, likely due to both cross-patient tumor microenvironment heterogeneity and preprocessing of scRNA-seq reads for quality control. After splitting the dataset into malignant and non-malignant cells and reducing the variables to just 35 redox genes represented in our quinone cycling systems model, t-SNE clustering revealed malignant cells tend to cluster by patient (Figure 2a), suggesting that there are distinct, patient-based tumor redox profiles. After clustering and shading samples by gene expression, we observed that while interpatient heterogeneity is likely the cause for patient-specific clustering, inpatient heterogeneity still existed and could be a source of why cells within a tumor can have different drug responses. This heterogeneity was observed when inspecting NQO1, GLUD1, TXN, and TXNRD1 expression (Figures 2b, 2c, 2d, and 2e). GLUD1 was included due to its ability to generate high production rates of NADPH as demonstrated by flux balance analysis studies (112). With this knowledge of heterogeneity between and within patient tumors, we leveraged redox transcriptional profiles per cell per patient to explore potential H₂O₂ buildup on cell- and tumor-based scales.

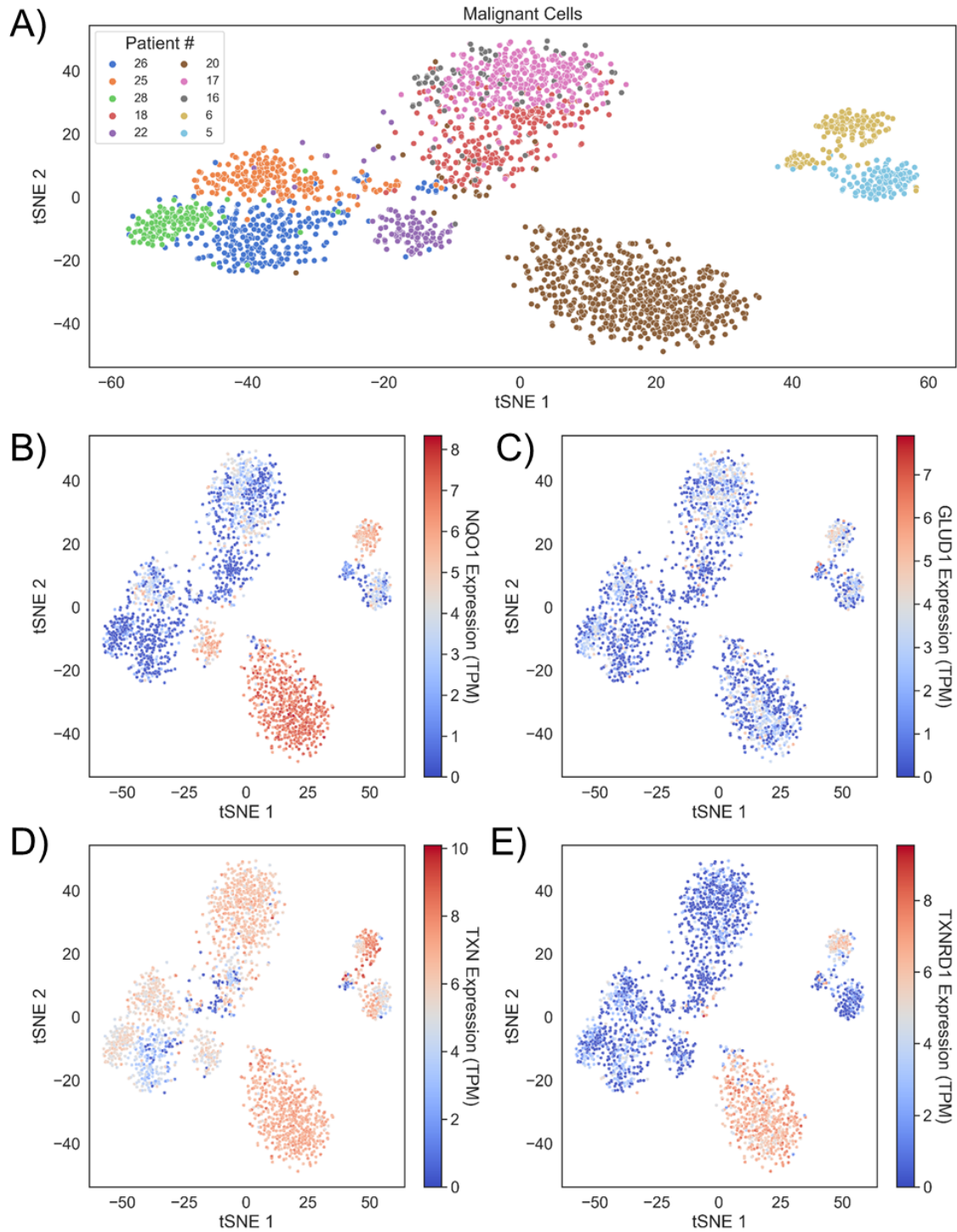


Figure 2: Head and neck cancers demonstrate intratumor and intertumor redox heterogeneity. A) Malignant cells from 10 HNSCC patients cluster together based on redox profiles. B) Clusters colored by NQO1, C) GLUD1, D) TXN, and E) TXNRD1 expression.

3.3.3 Initializing single cell ODE models with scRNA-seq

While scRNA-seq data has been widely used for exploratory data analysis and to understand gene expression correlations within developing tissues and cancer, this form of characterization has only recently been used to inform mechanistic kinetic models (113). We generated unique cell-based ODE systems using the previously analyzed scRNA-seq data. With the redox transcriptional profiles of almost 5000 cells from 10 patients, we first estimated the redox protein profiles as previously described (110,114) and imported these protein concentrations and related rate constants into our ODE model followed by simulation of the redox metabolism for each cell undergoing acute H₂O₂ generation by β -lapachone treatment. Specifically, AQP3, GSR, TXNRD1, NQO1, SOD1, POR, G6PD, and GLUD1 expression levels were used to adjust reaction rate constants by multiplying the rate constants by the percent change in the single cell expression from the average. G6PD and GLUD1 both generate NADPH and were combined into a single reaction in the model, and the impact of their expression levels on the kinetic rate constant was additive. GPX1, CAT, PRX1, PRX2, TXN, and GLRX expression levels were used to estimate initial enzyme abundances. PRX1 and PRX2 expression levels were combined to represent a single reaction in the model, and the impact of their expression levels on the initial enzyme abundances was additive. All other parameters and species levels were kept from prior modeling (97).

3.3.4 Sensitivity analysis shows H₂O₂ production is insensitive to individual enzymatic parameters

After constructing the ODE system, we sought to understand how influential each simulation parameter was on our system by performing a sensitivity analysis. We assessed the effect on intracellular H₂O₂ as the output variable of interest by altering model parameters up or down 10%. With most sensitivities remaining below 1 and H₂O₂ only being somewhat sensitive to several parameters, we concluded that no single parameter could alter the H₂O₂ production significantly (Figure 3a).

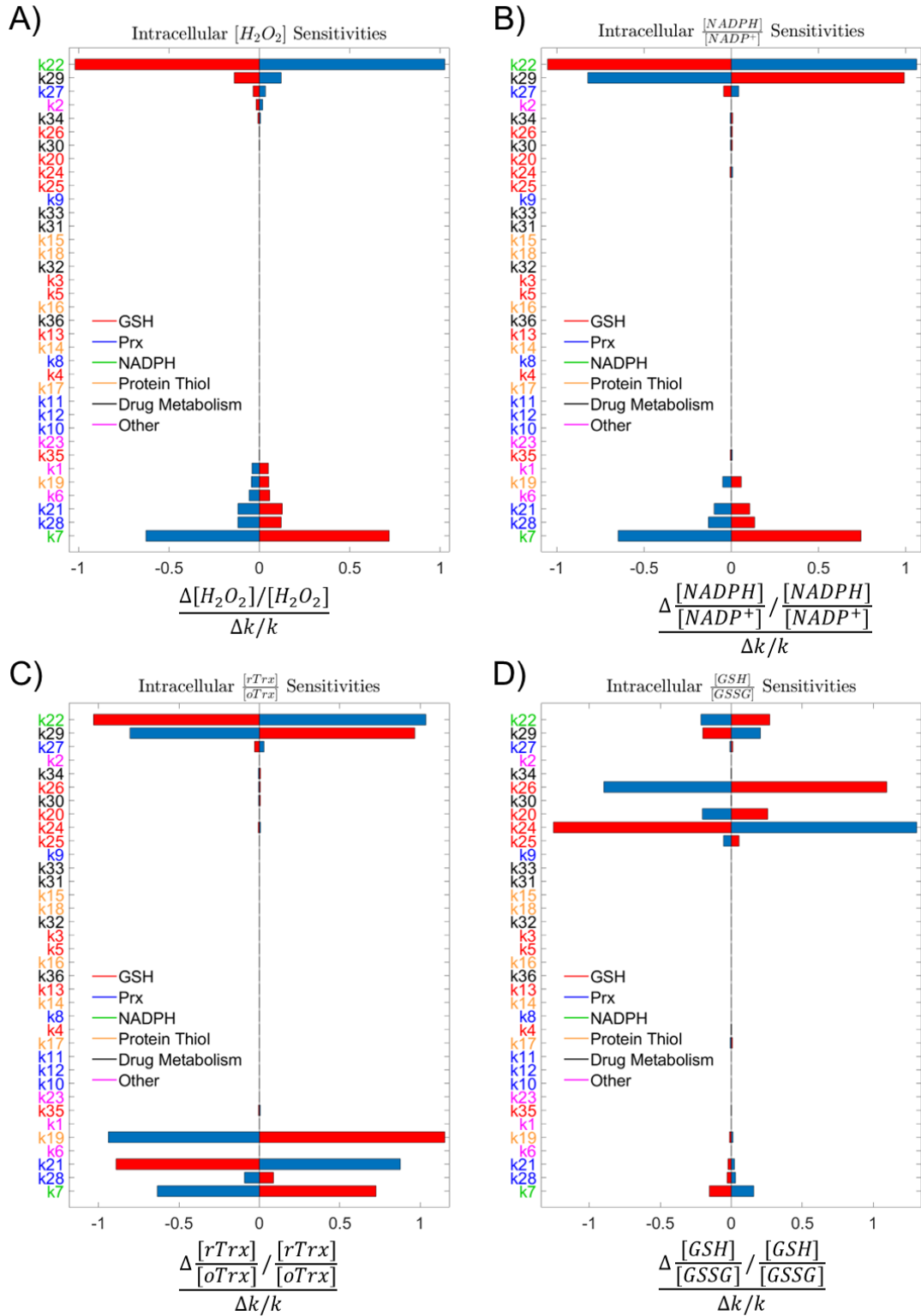


Figure 3: Sensitivity analyses. A) Analysis of system sensitivity to single parameter 10% perturbations colored by antioxidant subsystem shows low sensitivity of A) intracellular H_2O_2 , B) NADPH:NADP+, C) Trx-SH:Trx-SS, and D) GSH:GSSG at 2 hours to any single parameter.

Blue bars represent an increase in the parameter by 10% and red bars represent a decrease in the parameter by 10%.

Parameter labels colored by antioxidant subsystem also indicate no single antioxidant system is controlling a majority of the H_2O_2 scavenging load. Expanding the number of outcomes to include redox ratios of NADPH to NADP^+ , reduced thioredoxin to oxidized thioredoxin, and reduced glutathione to oxidized glutathione allowed us to assess the impact of these parameters on alternative indicators of redox status within the cell. The distribution of parameter importance in the sensitivity analyses across multiple redox mechanisms suggests that the reductive capacity of a cell is robust, and no single antioxidant enzyme system is predominantly responsible for clearance of H_2O_2 (Figure 3b-d).

3.3.5 Comparison of H_2O_2 accumulation in healthy and cancer cells identifies patients with greatest potential for targeted therapy

Using this new system of generating single cell ODE models, the redox profiles of individual cells within HNSCC can vary greatly and result in a range of H_2O_2 spanning many orders of magnitude. After removing simulations that were unstable, we had 4,243 single cell simulation outputs across all ten patients. All of the ten patients showed a trend of more H_2O_2 generated by the malignant cells relative to the normal cells, with seven patients exhibiting a statistical difference (Figure 4a).

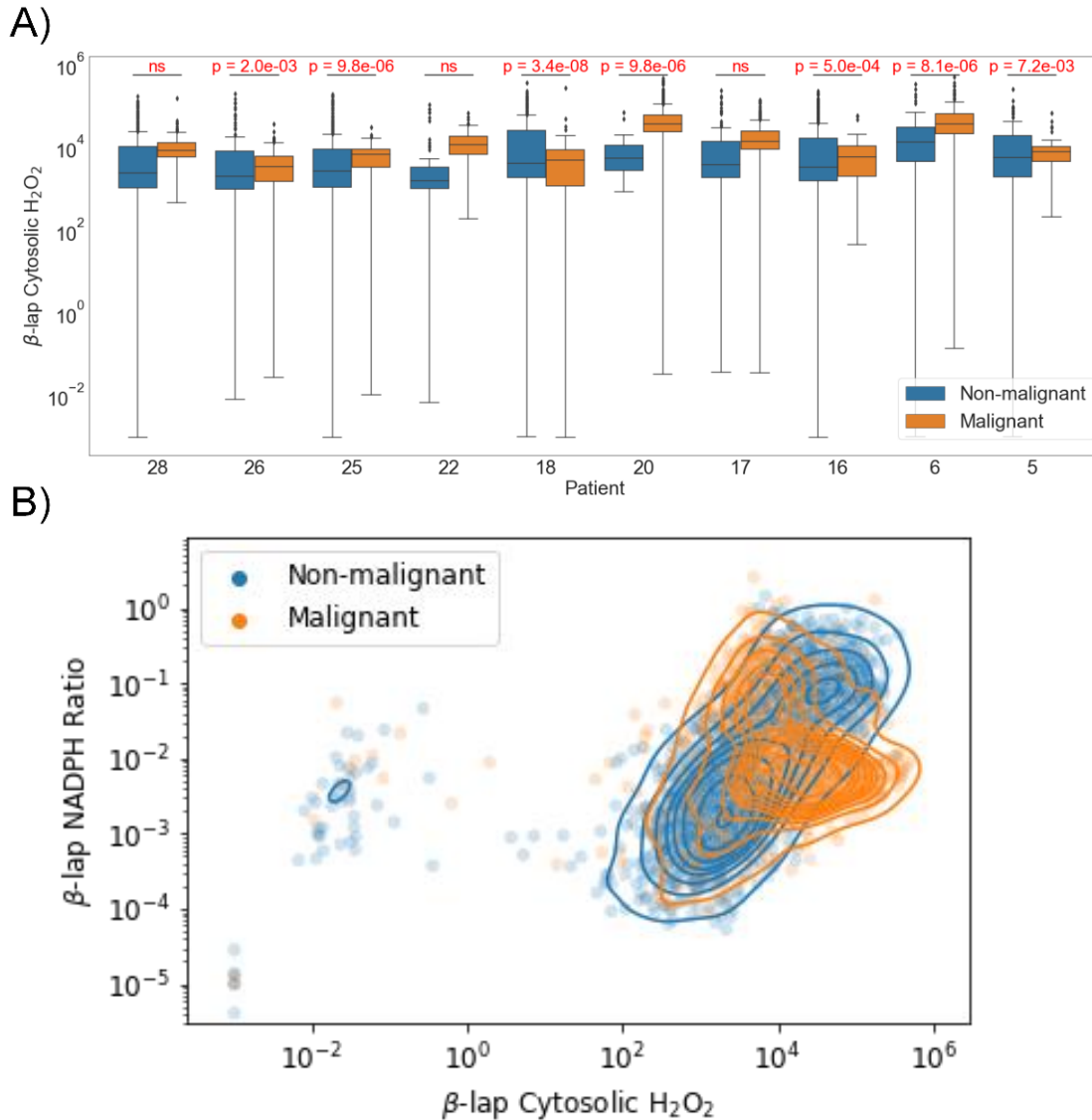


Figure 4: Model results using single cell gene expression values. A) Differences between cytosolic H_2O_2 in healthy and malignant cells under β -lapachone by patient. Boxes are defined by the interquartile range (IQR) with the line inside representing the mean. Upper whiskers are defined by adding 1.5 times the IQR to the third quartile and lower whiskers are defined by subtracting 1.5 times the IQR to the first quartile. Black diamonds represent outlier samples outside the whiskers. B) Differences between NADPH:NADP⁺ ratio and cytosolic H_2O_2 in healthy and malignant cells under β -lapachone.

Additionally, when comparing both H_2O_2 output and endpoint NADPH:NADP⁺ ratios across the 4,243 cellular models, we generally see higher H_2O_2 levels in cancer cells but no clear trend in NADPH:NADP⁺ ratios (Figure 4b). The denser malignant population

may indicate tighter redox regulatory control amongst the malignant cells. Alternatively, the less dense non-malignant population may simply reflect the fact that it includes all other cell types within the tumor (e.g. tumor-infiltrating T lymphocytes, macrophages, stromal cells). This shift demonstrates a potential for using single cell profiling to select patients for treatment with this targeted chemotherapy based on their redox profile. For the three patients where treatment induced H_2O_2 in both healthy and malignant cells without a statistically significant difference, the therapy may induce normal tissue toxicity impacting treatment and long-term quality of life.

3.3.6 Initializing single cell ODE models with patient HNSCC scRNA-seq identifies proteins most correlated with H_2O_2 production

Cytosolic NADPH redox ratio after a 2 hour simulation was collected and used in partial least squares regression to probe the correlations between the protein concentrations within the model and the output variable. With 4 and 3 components, respectively, both the malignant and non-malignant regression models are able to achieve both high explained output variance (non-malignant $R^2Y = 0.891$, malignant $R^2Y = 0.871$) and goodness of prediction (non-malignant $Q^2 = 0.886$, malignant $Q^2 = 0.858$). VIP scores identify NQO1, GLUD1, AQP3, TXN, and G6PD as the most important variables in the malignant model (Figure 5a) and GLUD1, NQO1, G6PD, POR, and GPX1 as the most important variables in the non-malignant model (Figure 5b). An interesting result is that GLUD1 has a higher VIP score in the non-malignant cells than NQO1, indicating that the outcome of drug treatment in non-malignant cells is more dependent on the production capacity of NADPH than the expression of the NADPH-reducing enzyme involved in the drug metabolism

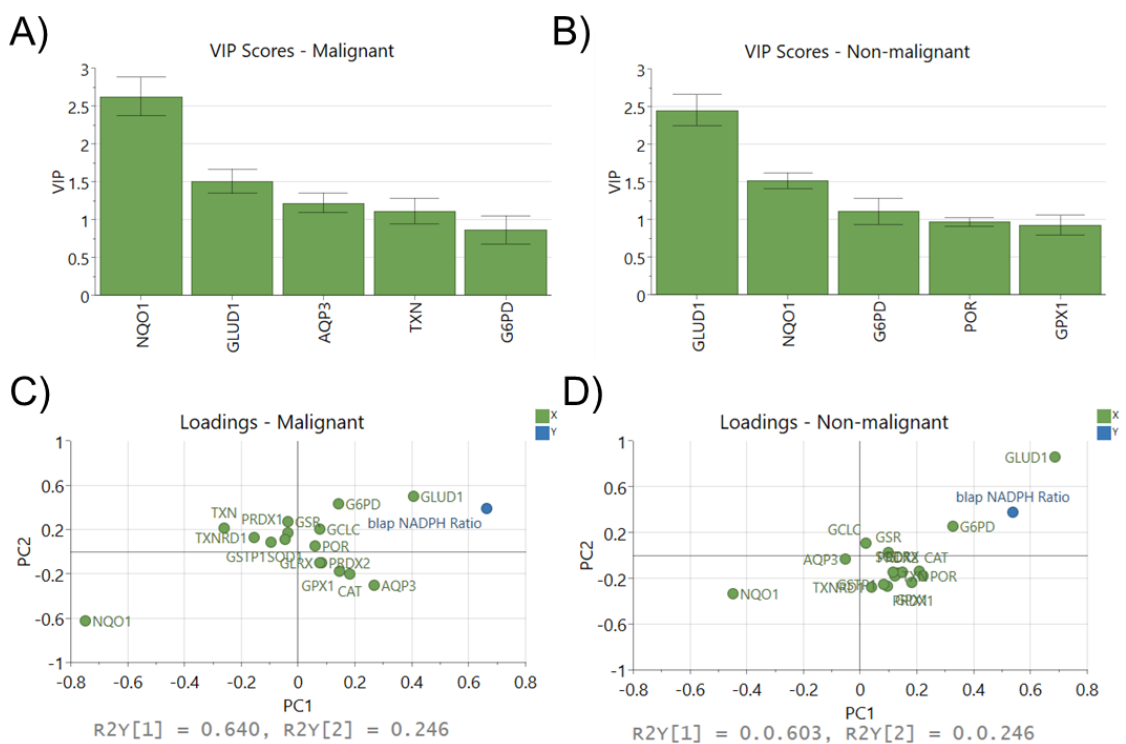


Figure 5: Partial least squares regression VIP scores and loadings. A) Genes with top 5 VIP scores in PLSR model in malignant simulations and B) non-malignant simulations. C) Breakdown of output into individual variables and loadings for each X and Y variable in malignant PLSR model and D) non-malignant PLSR model.

Collectively, the distribution of redox enzymes across principal components 1 and 2 differ between the two statistical models (Figure 5c,d) but there are several similarities. The distribution of NQO1 and CAT loadings in latent space reflects prior reports of NQO1/CAT not correlating well with LD50 values of β -lapachone across a diverse HNSCC panel (105). Additionally, the importance of AQP3 in the malignant model demonstrates the impact that diffusion of H_2O_2 across the cell membrane can have on the oxidative stress within a cell. NADPH-producing enzymes GLUD1 and G6PD and the main drug metabolizing enzyme NQO1 are most correlated with NADPH ratios, and most other antioxidant enzyme expression levels are less important due to low magnitude of their loading weights, i.e. proximity to the origin (Figure 5c,d).

3.4 Discussion

Because the main mechanism of action by NQO1-activatable drugs is the generation of superoxide and H_2O_2 , the ability for a cancer cell to manage these oxidants is a critical metric for chemotherapeutic response. NQO1:CAT ratio has been proposed as a predictive variable of NQO1-activatable drug success, but the utility of this metric is debated. Bey et al. in 2013 first speculated that NQO1:CAT could be useful after finding the use of exogenous catalase reduced the effects of β -lapachone in breast cancer (47), and higher NQO1:CAT were observed in NSCLC tumors that responded to treatment than in matched healthy tissue (45). In 2017 it was reported that the LD_{50} of β -lapachone did not correlate with NQO1:CAT in head and neck cancer (105). Additionally, while NQO1:CAT was not directly measured, inhibition of catalase and GSH did not lead to a sensitization of KEAP1-mutated NSCLC during β -lapachone treatment while inhibition of TXNRD and SOD1 sensitized cancers (50). A recent TCGA analysis revealed higher NQO1:CAT levels in hepatocellular carcinoma (HCC) than in matched healthy tissue, and the authors reported that the high NQO1 patient cohort had lower survival (115). These studies serve to highlight the complexity of the antioxidant system in the context of NQO1-activatable drugs like β -lapachone and suggest the current approach for identifying how well a cancer would respond to the treatment is underdeveloped. In this report, we generated a more accurate model of superoxide and H_2O_2 generation and scavenging under β -lapachone conditions by including additional antioxidant systems in an ODE-based approach in which H_2O_2 generation is a surrogate for drug potency. Including additional antioxidant systems and the kinetic information of enzymes simultaneously allowed us to predict measures other than NQO1:CAT that can serve as an indication of β -lapachone success.

When building a model to represent a biological system, there are always simplifications and assumptions that must be made using field expertise. Transcriptional regulation of the Keap1-Nrf2 axis on the scale of hours to days is not accounted for, in which the positive feedback of H₂O₂ activation of Nrf2-targeted genes results in enhanced NQO1 expression (116,117). Another major assumption used was that mitochondrial antioxidant systems would not reduce the large amount of H₂O₂ in this chemotherapeutic context due to the cytosolic location of NQO1 (118). Work done by Ma et al. shows that mitochondrial-targeted β -lapachone produces mitochondrial superoxide using MitoSOX, while 3-hydroxy β -lapachone which is not mitochondrially targeted produces no substantial mitochondrial superoxide (119). This allowed us to omit antioxidant enzymes expressed in the mitochondria such as SOD2, PRDX3, PRDX5. We did, however, find relatively high sensitivities of H₂O₂ permeabilities in the model, indicating the importance of how quickly a cell can export H₂O₂ during treatment. While H₂O₂ can passively diffuse through the phospholipid bilayer, it is also known to utilize aquaporin membrane proteins to travel through the plasma membrane (120–123). Because of the high sensitivities, measuring aquaporin expression levels could serve as a useful indicator of β -lapachone success.

When generating enzymatic models, protein activity levels are ideal but expression levels of proteins can be used to assume activity and can be acquired experimentally or from published datasets of other scientists' experiments. We chose an alternative strategy by estimating protein abundance based on the scRNA-seq mRNA levels. Because transcriptional levels do not directly correlate to protein levels, we used a quantitative pipeline to estimate protein abundances that leverages previously published data from

Schwanhausser et al (110,124). This allowed us to generate an ODE system specific to each cell sequenced in the scRNA-seq data. From our initial exploration of the scRNA-seq data, we observed the cells cluster by patient regardless of if they were healthy or cancerous similar to the results of an analysis conducted by Xiao et al. (125), so we concluded that each tumor was composed of a population of cells that were similar in redox profile. Yet when analyzing the expression of each antioxidant enzyme within these clusters, the overall antioxidant capacity or diversity of each tumor was unclear due to varied levels of each antioxidant enzyme.

Our ODE model was able to stratify the patient tumors based on the differences in the expected response of healthy and cancerous cells to β -lapachone, shedding some light on the complex nature of redox systems. Because we used scRNA-seq data that had transcriptomes of both normal and cancerous cells, we were able to assess the relative dependence of these two cell populations on their antioxidant enzyme expression under oxidative stress. As support of the consensus within the redox biology community that cancers experience higher levels of oxidative stress, we did see higher average levels of H_2O_2 within the cancer cell populations compared to the healthy cell populations within a given patient tumor. This result gave us confidence as a type of validation for the model and method we used. Additionally, the fact that some patients had significant differences between these healthy and malignant cell populations while others did not reinforces the notion that this drug can be used in a personalized manner for those patients that would have significantly higher levels of H_2O_2 in the cancerous cells than in the healthy cells. When the contours of the two cell populations are plotted in a 2D phase space of the two output variables, cytosolic H_2O_2 and NADPH ratio, we find these overlap quite closely,

but the cancer cell range is more compact. This suggests the cancer cell antioxidant phenotype can lead to a more controlled range of concentrations of H_2O_2 and reducing cofactors in oxidative environments, which can be seen as a survival advantage of the cancer cells. Similarly, while our comparisons of healthy and cancerous cells' redox state after treatment were of the aggregated samples in each population per patient, there is wide variability within each group and some healthy cells show a more oxidatively stressed state than cancerous cells in the same tumor. The healthy cells represent a repertoire of components found in the tumor microenvironment ranging from fibroblasts to macrophages, and thus a diversity of responses to an oxidative insult is expected. While cancer cells are typically seen as being more oxidized, these results predict that tumor heterogeneity assessed at a single cell resolution can potentially challenge narratives established using bulk-based characterization.

After breaking down the ODE model results into enzyme-specific impacts with PLSR, we found that the top five most important enzymes in both the malignant and non-malignant models included NQO1, GLUD1, and G6PD. This indicated that both the drug-metabolizing enzyme itself and the enzymes that produce the main redox cofactor involved, NADPH, were crucial to determining impact of the drug on a cell's redox state. Additionally, GLUD1 showing higher importance than NQO1 in the non-malignant model suggests that the production capacity of NADPH has a higher impact on the cell's redox state than the expression of the actual enzyme metabolizing the drug. AQP3 appearing as a VIP enzyme in the malignant cell model is another interesting finding that suggests that if a cancerous cell can allow more H_2O_2 to leave the cell via AQP3, it will be able to

maintain a better redox state. However, this finding implicates that malignant cells can produce and export H₂O₂ that can then go on to oxidatively stress neighboring cells.

A current issue with scRNA-seq data is a large volume of dropouts which leads to imputed values that are not true data (126). Dropouts in the context of single cell sequencing data refers to a lack of read counts for genes that may or may not be an accurate representation of the gene expression. These occur due to the fact that single cell sequencing is technically prone to not capturing every mRNA molecule within a cell while sequencing. Methods for both higher quality sequencing and imputation are being developed, and as higher quality datasets are published this model can be updated to reflect that (127,128). Additionally, the added value of spatial information from new spatial omics technologies could further improve the model. With the model currently representing a single cell system, a multicellular model of all of the cells simultaneously with physical parameters included could better represent the tumor system and buildup and breakdown of ROS. Lastly, our model only predicts how these cells within patient samples would respond to β -lapachone. Working with directly validated samples is a more ideal workflow, and we look forward to testing these models' accuracies if clinical data is made available in the future.

Altogether, this analysis demonstrates that developing an extensive enzymatic model of H₂O₂ generation and clearance using scRNA-seq data has the potential to identify the relative importance of various axes in the complex antioxidant network. We suggest that metrics other than NQO1:CAT should be considered when characterizing a HNSCC tumor and its capacity to respond to β -lapachone. These metrics include expression of TXN, GPX1, POR, and NADPH-producing enzymes such as G6PD and GLUD1.

Ultimately, the systems approach outlined here demonstrates the value of utilizing mechanistic modeling in conjunction with omics data to attain a more comprehensive understanding of the cellular redox state.

CHAPTER 4 EXPERIMENTAL QUANTIFICATION OF PERTURBATION EFFECTS ON β -LAPACHONE METABOLISM IN HEAD AND NECK SQUAMOUS CELL CARCINOMA

4.1 Introduction

Antioxidants within cells are capable of handling high levels of reactive oxygen species (ROS), and there are a wide array of antioxidant enzymes within each cell. When treating cells with β -lapachone it can be valuable to understand which experimental perturbations can be used to enhance the potency of the drug as a potential combination therapy. Previous work in non-small cell lung carcinoma (NSCLC) addressed the question of Nrf2/Keap1 mutations on β -lapachone cytotoxicity (42). The authors found that the cells had NQO1 overexpression due to Keap1 mutations, but inhibiting Nrf2-regulated antioxidants thioredoxin reductase 1 (TXNRD1) and superoxide dismutase 1 (SOD1) led to a sensitization of the NSCLC cells to β -lapachone. Interestingly, depletion of catalase or glutathione was not effective in reducing the resistance to β -lapachone. In this chapter, we used RNA silencing to assess the impact of perturbations on the ability of β -lapachone to produce H_2O_2 .

4.2 Materials and Methods

4.2.1 Cell Lines and Culture

HNSCC cell lines SCC-61 (Dr. Ralph R. Weichselbaum, The University of Chicago), rSCC-61 (129), SQCCy1 (Cellosaurus RRID:CVCL_0551), and shNQO1 SQCCy1 (Dr. David Boothman, The University of Indiana) were cultured in DMEM-F12

cell culture media with L-glutamine (Caisson Labs, Cat#DFL15) with 10% FBS (Sigma-Aldrich, Cat#F4135) and 1% Pen/Strep (Caisson Labs, Cat#PSL01) at 37°C and 5% CO₂. Cell media was changed every other day and cultures were passaged at 80% confluence and regularly tested for *Mycoplasma* (MycoAlert PLUS, Lonza, Cat#LT07).

4.2.2 siRNA Transfection

Cells were seeded in the wells of a black clear-, flat-bottom 96-well plate (Corning, Cat#3603). After one day, cells were washed three times with PBS and siRNA packaged in lipid nanoparticles using the N-TER Nanoparticle siRNA Transfection System (Sigma-Aldrich, Cat#N2913) was applied to each well at 50 nM in 100 uL of serum-free media for 4 hours. After this, an equal volume of media with 2X FBS (20%) was added for the remaining 20 hours of transfection. For each gene, three of the top-performing pre-designed MISSION siRNA constructs from Sigma-Aldrich were pooled and transfected concurrently. The transfection efficiency of these siRNAs against GAPDH has been performed previously (110) via Western Blot, and we repeated similar validation Western Blots with the pooled siRNAs against NQO1, a critical enzyme within our system. After 24 hours of transfection by siRNA, cells were washed three times with PBS and further experiments performed.

4.2.3 Amplex Red Measurements

Following siRNA transfection and PBS washes, Amplex Red and Horseradish Peroxidase (HRP) (Thermo Fisher Scientific, Cat#A2188) were added to the wells and kinetic fluorescent reads of resorufin (excitation 571 nm, emission 585 nm), the product of Amplex Red and H₂O₂ in the presence of HRP, were taken to measure H₂O₂ over time. After 10 minutes of reads to determine baseline extracellular concentrations of H₂O₂, 3 μM

of β -lapachone (synthesized in Boothman Lab, Indiana University) was applied to cells in serum-free media and reads were taken for 2 hours.

4.3 Results

4.3.1 Co-culture of NQO1 knockdown and wildtype cells shows dependence of H_2O_2 buildup on NQO1 expression.

We co-cultured SQCCy1 cells and SQCCy1 cells with stable shNQO1 transfection at various proportions, treated them with β -lapachone, and measured H_2O_2 levels over time for 2 hours. The shNQO1 cells by themselves were capable of producing H_2O_2 , but the wildtype cells produced over 2 times the amount (Figure 6). As the proportion of wildtype cells increased from 25% to 100%, the total H_2O_2 produced also increased in a linear fashion.

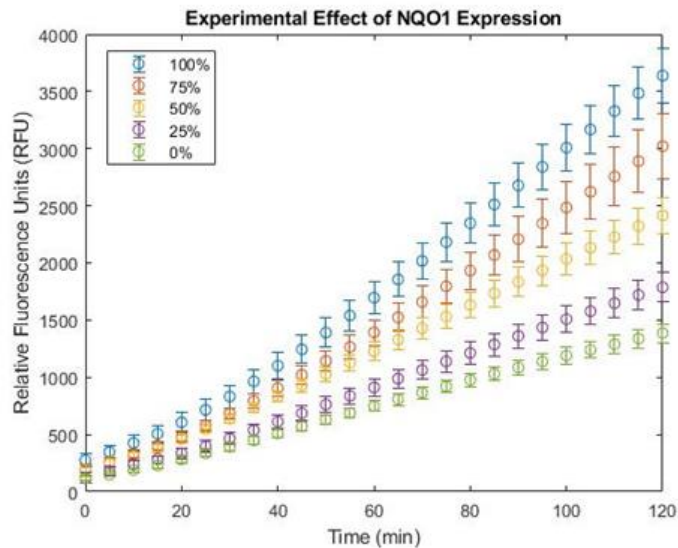


Figure 6: H_2O_2 buildup over time during β -lapachone treatment based on amount of NQO1⁺ cells.

Bars show +/- std.

4.3.2 Experimental knockdown of NQO1 shows changes in levels of NQO1, Nrf2, and PRDX1.

We assessed the efficiency of 24 hour siRNA knockdowns in rSCC and SCC cells using Western blotting. We found that knocking down NQO1 led to a 40% and 50% reduction in NQO1 in SCC and rSCC cells, respectively (Figure 7a-b). We also found that knocking down other enzymes involved in H₂O₂ reduction such as Nrf2 and PRDX1 also led to changes in NQO1. In rSCC cells, knocking down Nrf2 led to a 30% reduction in NQO1, but in SCC cells, knocking down Nrf2 surprisingly led to a 20% increase in NQO1 levels. Knocking down PRDX1 in SCC cells also led to a 20% increase in NQO1 levels and a 50% increase in NQO1 in rSCC cells. These changes to protein levels that were not specifically targeted with siRNA suggest either a global siRNA impact on ROS-related protein expression as demonstrated by Kippner et al. (130) or an indirect, downstream effect of these proteins on overall redox state. One possibility is that lowering Nrf2 or PRDX1 can increase basal ROS levels resulting in the production of antioxidant enzymes such as NQO1 through other mechanisms. To put these changes into more context, the SCC cells had much lower levels of NQO1 overall relative to rSCC cells, so the changes in rSCC cells were much greater in absolute terms (Figure 7c).

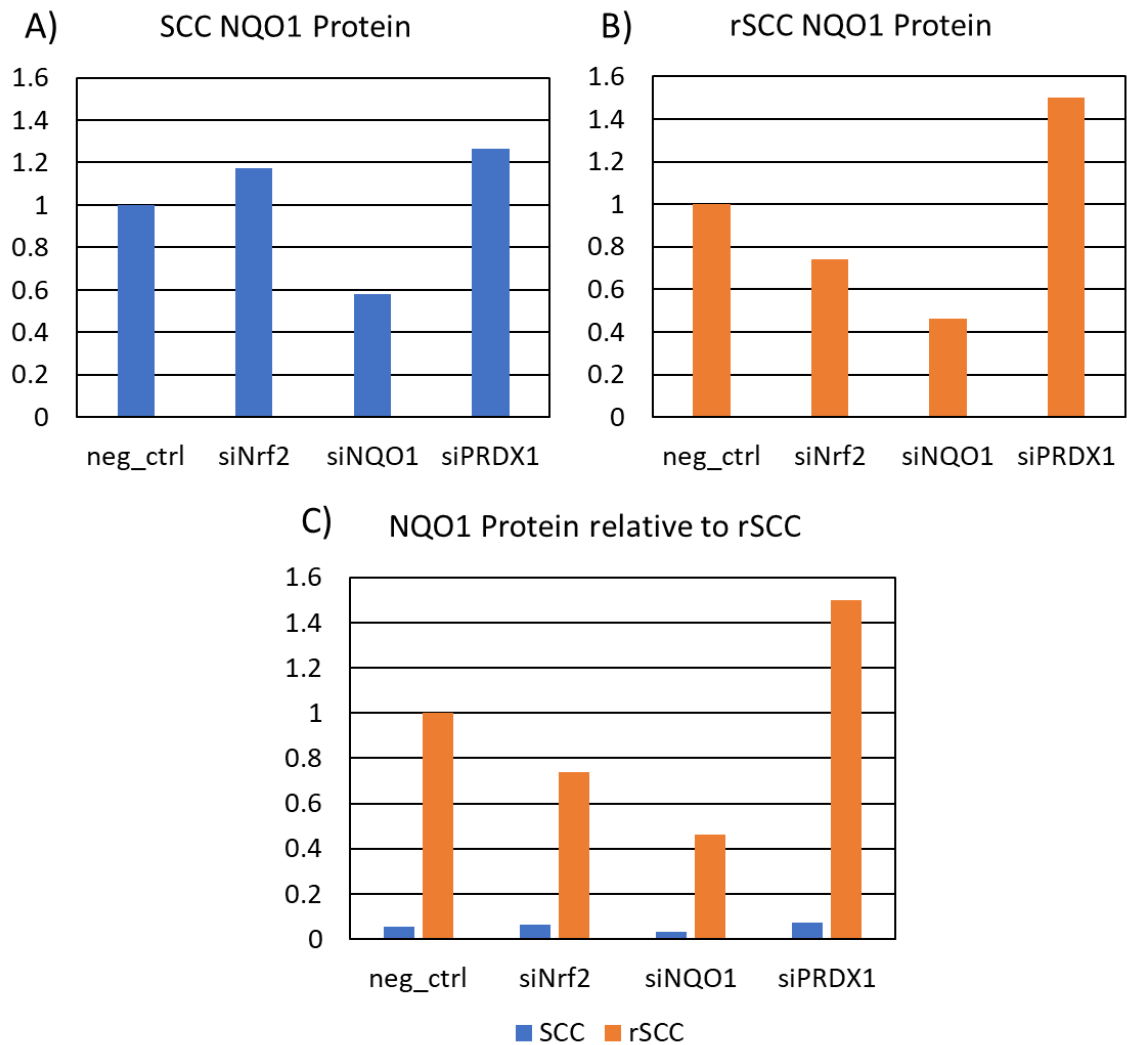
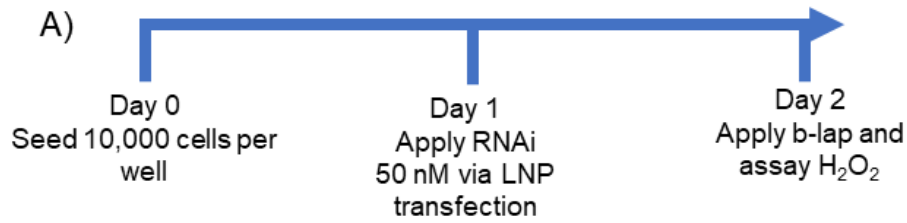


Figure 7: NQO1 expression levels after siRNA knockdown.
 A) Levels of NQO1 in SCC cells after siRNA knockdowns of Nrf2, NQO1, and PRDX1. B) Levels of NQO1 in rSCC cells after siRNA knockdowns of Nrf2, NQO1, and PRDX1. C) Relative levels of NQO1 in SCC and rSCC cells after siRNA knockdowns of Nrf2, NQO1, and PRDX1.

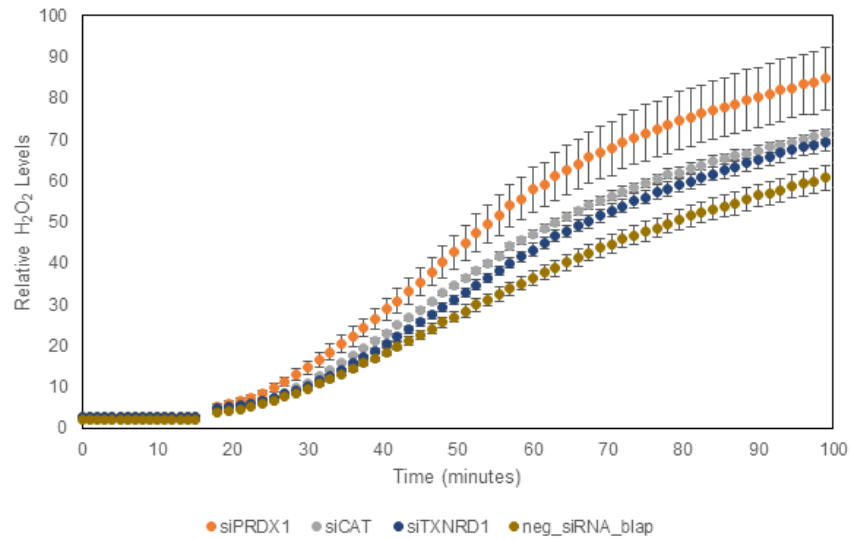
4.3.3 Experimental knockdown of antioxidant enzymes shows lack of effect on H₂O₂ buildup.

We used siRNA to perturb antioxidant enzyme levels and then observed the knockdown effect on acute H₂O₂ production induced by β-lapachone over a 100 minute

period (Figure 8a). After confirming pooled siRNA silencing, we individually silenced proteins within a set of antioxidant or antioxidant-related enzymes including CAT, GPX1, GPX4, SOD1, GSR, PRDX1, TXN, TXNRD1, GLUD1, and G6PD to explore their impact on H₂O₂ production during β -lapachone treatment. We hypothesized that knockdown of antioxidants would result in an increase in H₂O₂, while knockdown of NQO1 would reduce drug metabolism and therefore H₂O₂ levels with β -lapachone treatment would be lower. We used Amplex Red to probe extracellular H₂O₂ levels over the course of 2 hours of drug treatment and compared the fold change in H₂O₂ relative to control scrambled siRNA (Figure 8b,c). With the maximum fold change no greater than 30% at 2 hours and relatively large standard deviation, these single knockdowns did not impact the redox state of the cells significantly by Welch's t-test, confirming our simulated parameter sensitivities.



B) Relative H_2O_2 Levels after knockdown of Key Proteins



C) Redox Enzyme siRNA Knockdown

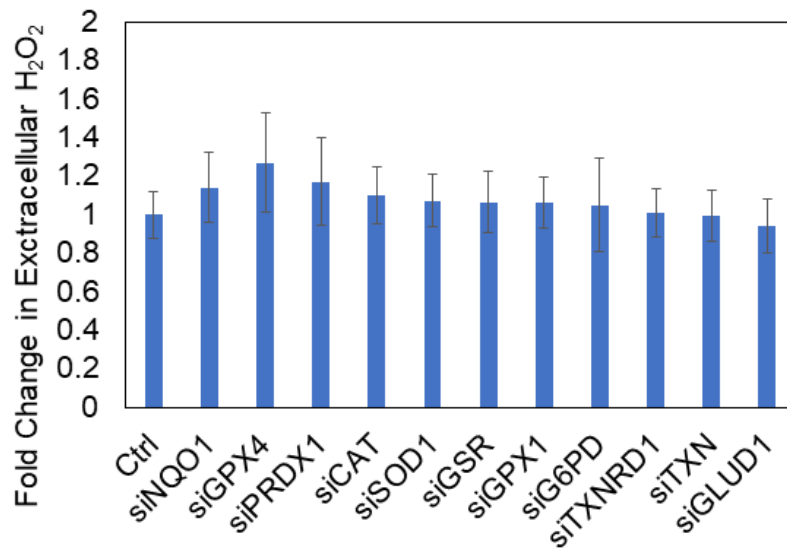


Figure 8: siRNA perturbation studies validate sensitivity analyses. A) siRNA knockdown workflow. B) Kinetic reads of H_2O_2 for PRDX1, CAT, and TXNRD1 enzyme knockdowns in a representative experiment showing increase in H_2O_2 after antioxidant knockdown (mean \pm s.d.).

C) Aggregated fold change in H_2O_2 at 2 hours for each antioxidant knockdown shows limited increase in H_2O_2 confirming computational sensitivity analyses (mean \pm s.d.).

4.4 Discussion

The impact that perturbing the antioxidant system and the method in which it is done has on the potency of β -lapachone in HNSCC is poorly understood. In this chapter, we compared how protein expression levels and protein inhibition could impact the production of H_2O_2 in HNSCC after β -lapachone treatment. We utilized matched cell lines with one having a stable NQO1 knockdown via shRNA to analyze differences in H_2O_2 buildup, and we tested the impact of transient knockdown of NQO1 and other antioxidant enzymes on H_2O_2 buildup and NQO1 levels. Overall, we found transient knockdowns of antioxidants did not impact the effects of β -lapachone using H_2O_2 buildup as an indicator. Interestingly, when we co-cultured cells that either endogenously expressed NQO1 or had stable knockdown of NQO1, we did find H_2O_2 buildup was dependent on the proportion of cells that expressed NQO1.

The fact that transient siRNA had almost no effect on the buildup of H_2O_2 and the stable shRNA knockdown showed a clear relationship between amount of knockdown cells and wildtype cells on the buildup of H_2O_2 can be attributed to differences in these methods of gene silencing (131). The creation of a stable shRNA cell line is done through selection and therefore ensures each cell would have a knocked down NQO1 gene. While we did show overall levels of NQO1 go down through siRNA transfection, it is unclear whether the expression of NQO1 is decreased for all cells or if only the overall amount of NQO1 goes down as a result of some cells being successfully transfected and others not taking up the siRNA liposome. Additionally, siRNA has been shown to have more off-target effects than shRNA which can lead to more altered gene expression in the siRNA treated cells which can make it difficult to determine the specific effects of siRNA gene knockdown (132). Additionally, we see some of these off-target effects in the NQO1 Western blots while silencing genes other than NQO1. Knocking down Nrf2 and PRDX1 was capable of influencing the protein expression level of NQO1 in rSCCs and SCCs.

Altogether, in this chapter we showed that while NQO1 levels do affect the production of H₂O₂ when cells are treated with β-lapachone, perturbation methods including siRNA may not prove to be the optimal way to sensitize cells to β-lapachone. siRNA shows too many off-target effects and more specific small molecule inhibitors of these enzymes may be more appropriate.

CHAPTER 5 THE ROLE OF TUMOR ARCHITECTURE AND HETEROGENEOUS ANTIOXIDANT EXPRESSION ON β -LAPACHONE DRUG POTENCY

5.1 Introduction

Development of complex *in vitro* cancer tissue culture models has been a focus in the cancer biology field for the past few decades. One method of doing so is by generating 3D *in vitro* cancer tumorspheres. 3D cancer models are currently used to study how oxygen concentrations can affect viability and how cancer cells organize themselves in extracellular matrix (133,134). These 3D models have several advantages over conventional 2D *in vitro* methods and even *in vivo* animal studies (52). Models *in vivo*, such as genetically-induced mouse cancers or orthotopic xenografts of human tumors in nude mice, are thought to have potential limitations due to a lack of immune cells in xenograft tumor models and differences in telomerase regulation, cytokines, and metastatic rates between human and rodent cancers (135,136). Because of these differences, the development of advanced 3D patient tissue models has the potential to better represent human organ systems, even *in vitro*. The advantages over 2D *in vitro* models include being able to more accurately depict how tumors metabolize drugs, express genes and synthesize proteins, survive, and consume oxygen (57–61). Drug metabolism studies ideally should take into account spatial considerations of diffusion limitations in oxygen and nutrients (52–56).

Computational models can increase the throughput of testing theoretical conditions and attribute experimentally seen outcomes to variables that are difficult or impossible to measure experimentally. Previous 3D computational work using a discrete model described the formation of a capillary sprout network and demonstrated that intratumor drug concentrations can depend on vascularization (80), motivating the need to model how chemotherapeutic distribution leads to different drug metabolism within the tumor.

Another study by Anderson et al investigated how limitations of oxygen affected cell consumption and growth patterns; a key finding was that cells would increase their motility and move away from hypoxic regions and towards areas with higher nutrient availability (82). Building further on this work, agent-based models (ABMs) were developed to investigate the metabolism of hypoxia-activated prodrugs in heterogeneous tumors. The ABM analysis was extended to include the “bystander effect” in which the cells that could metabolize the drugs well would impact neighboring cells with less efficient drug metabolism. The authors reported that the extent of the bystander effect depended on which prodrug was applied and that penetration of the drug to the center of their tumors could pose a challenge for the more interior cells to be killed (86).

This bystander effect has not only been seen computationally, but experimentally in the context of a metabolically-activated drug, β -lapachone. β -lapachone relies upon high expression of NAD(P)H:quinone oxidoreductase 1 (NQO1) to cycle between quinone, hydroquinone, and semiquinone states, cycling over 60 moles of NADPH/mole of β -lapachone in 5 minutes releasing 20 mol/min of O_2^- inducing catastrophic NADPH depletion and oxidative stress as a mechanism for cell death (40,47). In triple-negative breast cancer cells 2D culture studies, NQO1⁻ cells near NQO1⁺ cells were affected during β -lapachone treatment as monitored by levels of DNA damage response marker gamma-H2A histone family member X (γ H2AX), and this effect could be blocked by exogenous addition of catalase (49). Notably, the number of lesions in surrounding cells were distributed in inverse square distance relation to metabolizing cells, reflecting the diffusion of hydrogen peroxide (H_2O_2) as the mechanism of DNA damage. NQO1⁺ cells died by programmed necrosis, while the neighboring NQO1⁻ cells underwent typical caspase-dependent apoptosis. This previous work on the bystander effect motivates the exploration of how NQO1⁺ and NQO1⁻ cells and their locations could impact overall drug potency and cell type specific viabilities in various tumor architectures.

In our own previous work, we used transcriptomic data to build single cell models of β -lapachone metabolism and decomposition of H_2O_2 within cancer cells (137). We included NQO1 metabolism and a wide range of antioxidants we knew to be relevant to oxidative stress. We concluded through multidimensional analysis that the metabolic model depicting this drug metabolism and subsequent reduction of its oxidative byproducts was dependent on three main aspects in the system: the production of oxidants by NQO1 metabolism, the decomposition of H_2O_2 by antioxidant enzymes, and the production of NADPH. These results led us to believe that assuming a reduced metabolic model within our overall ABM could bring down the computational cost of the model while retaining the critical aspects of the drug metabolism. Additionally, previous work with tumorspheres shows radial differences in both nuclear factor erythroid 2-related factor 2 (Nrf2) and hypoxia inducible factor 1 subunit alpha (HIF1 α) expression which imply spatial differences in antioxidant enzyme expression and oxygen tension, respectively, and further motivates the use of ABMs in redox-based tumorsphere studies (138).

To explore the role of spatial organization on β -lapachone bystander effects, here we describe simplified and complex ABMs to model the effects of β -lapachone on tumorspheres consisting of cultured cell lines. Our simulations allowed us to explore the effects of heterogeneity on drug metabolism and localized H_2O_2 accumulation. The simplified ABMs were used to determine the impact of the bystander effect on overall chemotherapeutic potency in populations of cells by comparing simulations with different tumor architectures. The more complex ABMs were initialized by experimentally-derived expression profiles and yielded predictions of O_2 and H_2O_2 concentration in the tumorsphere space. As previously mentioned, we assumed the comprehensive antioxidant system within cells could be represented in a simpler way than including each direct mechanistic enzyme reaction. Our complex model was built by experimentally probing for NQO1, catalase, and glutamate dehydrogenase 1/2 (GLUD1/2) which represent on a more abstract level the production of H_2O_2 , decomposition of H_2O_2 , and production of NADPH,

respectively associated with β -lapachone metabolism. GLUD1/2 was chosen due to its relevance in NADPH production as shown by Lewis et al. in 2021 (110). These two models suggest that the bystander effect, considered an important aspect for increased intratumor cytotoxicity, is limited in organized tumor pockets of high NQO1 expression during β -lapachone treatment. Overall, we demonstrate the impact that spatial organization of phenotypes within tumorspheres can have on viability during β -lapachone treatment. Knowing the overall composition of phenotypes within a tumorsphere is supplemented by the knowledge of spatial organization, and using computational models that include this spatial information can better represent treatment outcomes.

5.2 Materials and Methods

5.2.1 Cell Lines and Culture

Head and neck squamous cell carcinoma (HNSCC) cell lines SCC-61 (Dr. Ralph R. Weichselbaum, The University of Chicago) and rSCC-61 (129) were cultured in DMEM/F12 cell culture media with L-glutamine (Gibco, Cat#12400024) with 10% FBS (Sigma-Aldrich, Cat#F4135) and 1% Pen/Strep (Caisson Labs, Cat#PSL01) at 37 °C and 5% CO₂. Cell media was changed every other day and cultures were passaged at 80% confluence and regularly tested for *Mycoplasma* (MycoAlert PLUS, Lonza, Cat#LT07).

5.2.2 Generation and processing of spheroids to provide fluorescence microscopy samples

50,000 cells were plated in ultra-low attachment plates which resist adherence and promote spheroid formation in DMEM/F12 with 10% FBS. 6 replicates per condition were grown. The tumorspheres were grown with varying proportions of rSCC and SCC cells:

50/50% rSCC/SCC, 75/25% rSCC/SCC, 90/10% rSCC/SCC, and pure rSCCs. Prior to plating, rSCC cells were stained with 20 μ M CellTracker Red (ThermoFisher Scientific #C34552) for 30 minutes. After 2 days when spheroids are approximately 1–2 mm in diameter and visible to the naked eye, spheroids were washed with PBS carefully so as not to break them apart. After washing, spheroids were treated with 5 μ M β -lapachone for 2 hours, then spheroids were washed and fixed with 4% paraformaldehyde in PBS and for one hour. Cells were washed with PBS and carefully transferred to a cryomold, removing as much PBS as possible. 3–5 spheroids of the same condition were placed in the cryomold with minimal PBS, then covered with optimal cutting temperature (OCT) liquid. Subsequently, the spheroids were frozen by floating the cryomolds on the surface of isopentane chilled with liquid nitrogen until solid, about 2 minutes. Frozen cryomolds were stored until cryosectioned in -80 °C.

To section, frozen blocks were first equilibrated in the cryostat set at -20 °C for 30 minutes, then sectioned at a thickness of 10 microns and transferred to slides, which were stored at -80 °C until ready for immunostaining.

5.2.3 Immunofluorescence microscopy

Slides were equilibrated to room temperature for 30 minutes, and polypropylene chambers were superglued to each slide and allowed to dry for 10 minutes. For the first cycle of immunofluorescence, samples were permeabilized with 0.3% Triton-X in PBS for 10 minutes. Next, the samples were blocked with LICOR Intercept (PBS) Blocking Buffer for one hour at room temperature, followed by incubation with primary antibody cocktail in blocking solution at 4 °C overnight. The next day, the slides were washed with PBS for

10 minutes 3 times to remove excess primary antibody. Secondary antibodies were added at a 1:1000 dilution in PBS and incubated for one hour at room temperature. Slides were washed again as previously described and stained with Hoechst 33342 (Fisher Scientific #H3570) at a 1:10,000 dilution in PBS for 10 minutes then washed again. Samples were imaged immediately in PBS following the last wash. A fluorophore inactivation step, which involves incubation in 4.5 H₂O₂ and 24 mM NaOH for 1 hour at room temperature in the presence of strong light, was performed after each staining cycle. The catalase antibody (LS Bio #LS-B3014) was used at a 1:400 dilution and subsequently an Alexa Fluor 647-conjugated anti-goat secondary antibody (ThermoFisher Scientific #A-21447). The NQO1 antibody (Cell Signaling Technology #3187) was used at a 1:400 dilution and subsequently an Alexa Fluor 488-conjugated anti-mouse secondary antibody (ThermoFisher Scientific #A-11001). The Alexa Fluor 488-conjugated glutamate dehydrogenase ½ (GLUD1/2) antibody (abcam #ab204001) was used at a 1:100 dilution. The Alexa Fluor 647-conjugated γ H2AX antibody (BioLegend #613407) was used at a 1:200 dilution. Images were collected with the Nikon W1 spinning disk confocal microscope using a 20x air objective lens (Plan Apo Lambda) with a Hamamatsu ORCDA-Fusion Gen-III sCMOS camera. After tumorsphere processing and sample loss, we captured CycIF data for seven tumorspheres total: four 50% rSCC, one 75% rSCC, and two 90% rSCC.

5.2.4 Processing of microscopy images to collect single cell data

After microscopy, the nuclear stain from each cyclic immunofluorescence (CycIF) cycle for a given sample were registered using the methods described by Nikitina et al. (139), which were originally described in the context of aligning MALDI mass

spectrometry images with confocal nuclear images. Dual annealing was used to optimize a mutual information-based alignment score of the two nuclear images by translating, rotating, and scaling each image to best overlap with one another. As these images are much larger than the MALDI images originally intended for use with the mentioned methods, each cycle was resized and aligned at multiple scales from 6.5 $\mu\text{m}/\text{px}$ to the original scale of 0.33 $\mu\text{m}/\text{px}$ while decreasing the search range proportionately, obtaining progressively finer alignments in a resource-efficient manner.

For each spheroid, the highest-quality nuclear image was selected from the three cycles and single cells were segmented with a custom Python blob detection pipeline utilizing the multiscale Laplacian of Gaussian (LoG) algorithm (140). Objects with a radius in the range of 3.25 to 8.125 μm were identified as cells, while outliers were ignored. In order to quantify single-cell abundances, these contours were overlaid with each stain from each cycle, and the mean intensity for each nucleus was computed. The custom registration and segmentation Python scripts utilized OpenCV 4.5.4.58, SciPy 1.7, and scikit-image 0.19.1 for image preprocessing, alignment, and post-processing. NumPy 1.21.4, Pandas 1.3.4, matplotlib 3.4.3, tifffile 2021.11.2, and nd2 0.5.3 were used for data manipulation and file reading.

5.2.5 Analysis of spatial single cell data

Catalase, NQO1, GLUD1/2, γH2AX , and CellTracker Red intensity values in addition to cell locations were loaded into a Pandas dataframe. Values were standardized to be between 0 and 1. Euclidean distance from the center of the tumorsphere section was

calculated and added to the dataframe. The center of the tumorsphere was calculated as the average x and y values of the cells identified.

5.2.6 Extracellular concentration grids and diffusion

To simulate diffusion of O₂ and H₂O₂ simultaneously within the tumor spheroids under β -lapachone treatment, grids with 1 micron resolution were used. The concentration grid was solved using the forward time centered space numerical method, with the necessary time step for stability being calculated using von Neumann stability analysis. This time step is dependent on both the spatial resolution and the diffusivity of each species. To simplify this analysis, the maximum of the two species' diffusivities was used and the x and y spatial resolutions were identical. The equation for a stable time step is shown below in equation 2. Δt represents the time step, Δx and Δy represent the spatial resolution, and D_{max} represents the maximum diffusivity of the diffusing species.

$$\Delta t \leq \frac{1}{2D_{max}} * \left(\frac{1}{(\Delta x)^2} + \frac{1}{(\Delta y)^2} \right)^{-1} = \frac{(\Delta x)^2}{4D_{max}} \quad (2)$$

To update the concentration grid at each time step in the simplified ABM, the concentration of O₂ at grid points within cell radii was used to calculate the amount of O₂ consumed and H₂O₂ produced at those grid points depending on if the cells were NQO1⁺ or NQO1⁻ as described below. To update the concentration grid at each time step in the complex ABM, the concentrations of O₂ and H₂O₂ at the grid point closest to the center of each cell were used as the initial O₂^{extra} and H₂O₂^{extra} values within each cell's ODE model as described below. For both models a 2D Laplacian stencil made with the numba.stencil python library then convoluted the current concentration grid to simulate diffusion for one simulated minute with as many timesteps as the von Neumann stability analysis dictated.

5.2.7 Cell death mechanism

To simulate stochastic cell death, a function of intracellular H_2O_2 representing probability was used as shown below in equation 3. This is a Hill equation and depending on the hill coefficient can appear as a sigmoid curve or Michaelis-Menten saturating curve. Every simulated minute, each cell generated a random number; if the number was below the probability value, the cellular agent changed its state to dead and stopped intracellular metabolism, representing proteasomal degradation and cell death. The maximum function allowed for a threshold, so that cells below this concentration would not die. Hill represents the hill coefficient and threshold represents the minimum H_2O_2 value at which a cell can die.

$$P(\text{Death}) = \frac{\max([H_2O_2^{cyto}] - \text{threshold}, 0)^{Hill}}{\max([H_2O_2^{cyto}] - \text{threshold}, 0)^{Hill} + \text{threshold}^{Hill}} \quad (3)$$

5.2.8 Simplified ABM

A simple ABM was built using the pythonabm 0.3.1 library at <https://pypi.org/project/pythonabm/> and <https://github.com/kemplab/pythonabm> on a Windows 10 machine. Additions to the model simulation object were described previously including the diffusion and cell death mechanism modules. The simple ABM has two cell types: $NQO1^+$ and $NQO1^-$. $NQO1^+$ cells produced H_2O_2 with a rate constant of 0.06 1/s multiplied by the extracellular O_2 concentration within the cells' radius as a point source that fed into the extracellular concentration grid for diffusion. This rate constant was determined using previous research with H_2O_2 concentrations over time after β -lapachone treatment [19]. For each of the architectures there were 300 $NQO1^+$ cells and 300 $NQO1^-$

cells. For the concentric architectures, cell locations were chosen so that the cell density for each cell type was the same. The same cell death probability function was used for this ABM as described above.

5.2.9 Intracellular ODE model

For a more sophisticated treatment of context-dependent cell fate decisions, a coupled set of ordinary differential equations (ODEs) was nested in each cellular agent in what we refer to as the “complex ABM” model. Even so, only four species were included in the ODE network: O_2 , H_2O_2 , $NADP^+$, and $NADPH$, and we assumed that all cells in the system receive the same dosage of intracellular β -lapachone during the 2 hours of simulated treatment. O_2 and H_2O_2 are simulated in the intracellular and extracellular compartments of the ODE network. The extracellular compartment allowed for the description of membrane permeability to be included and for the ODE system to interact with the extracellular O_2 and H_2O_2 concentration grids used in diffusion solving. The concentrations at the grid point nearest the cell center were pulled for the initial ODE values for the extracellular component. After the intracellular ODE was solved per time step, the concentration grid points within each cell radius was updated to reflect the extracellular values solved for in the ODE. The ODE system is shown below in Table 1. There are 5 main terms found across the 6 ODEs. The reactions with parameters p_1 and p_2 represent the permeation of O_2 and H_2O_2 across the cell membrane, respectively and are driven by the difference in concentration across the cell membrane. These do not need volumetric compartment correction due to the concentration updates to the extracellular O_2 and H_2O_2 only occurring in the extracellular volume directly adjacent to each cell. The reaction with

k_1 represents the NQO1 drug metabolism that requires O_2 and NADPH and k_1 is approximated as a value between 0 and 1 determined by standardized NQO1 protein intensity per cell. The reaction with k_2 represents an abstract pooled antioxidant term requiring H_2O_2 and NADPH and k_2 is approximated as a value between 0 and 1 determined by standardized catalase protein intensity per cell. Last, the k_3 reaction represents an abstract pooled NADPH production term converting $NADP^+$ to NADPH and k_3 is approximated as a value between 0 and 1 determined by standardized GLUD1/2 protein intensity per cell.

Table 2: ODEs included in ABM intracellular model

Name	Initial Value (μM)	Differential Equation
O_2^{cyto}	260	$\frac{\Delta O_2^{cyto}}{\Delta t} = NADPH * (k_2 * H_2O_2^{cyto} - k_1 * O_2^{cyto}) + p_1 * (O_2^{extra} - O_2^{cyto})$
$H_2O_2^{cyto}$	0.001	$\frac{\Delta H_2O_2^{cyto}}{\Delta t} = k_1 * O_2^{cyto} * NADPH - k_2 * NADPH * H_2O_2^{cyto} + p_2 * (H_2O_2^{extra} - H_2O_2^{cyto})$
NADPH	30	$\frac{\Delta NADPH}{\Delta t} = k_3 * NADP^+ - NADPH * (k_1 * O_2^{cyto} + k_2 * H_2O_2^{cyto})$
NADP+	0.3	$\frac{\Delta NADP^+}{\Delta t} = NADPH * (k_1 * O_2^{cyto} + k_2 * H_2O_2^{cyto}) - k_3 * NADP^+$
O_2^{extra}	260	$\frac{\Delta O_2^{extra}}{\Delta t} = p_1 * (O_2^{cyto} - O_2^{extra})$
$H_2O_2^{extra}$	0	$\frac{\Delta H_2O_2^{extra}}{\Delta t} = p_2 * (H_2O_2^{cyto} - H_2O_2^{extra})$

5.2.10 Intracellular ODE parameterization

The CycIF data were quantified for determining individual cell parameter values. First, the cell locations were multiplied by the scaling factor $0.33 \mu m/px$ set during microscopy image processing to get their locations in microns. NQO1, catalase, GLUD1/2,

and γ H2AX values were standardized with min max scaling to be between 0 and 1. These normalized values for NQO1, catalase, and GLUD1/2 were used to determine the lumped parameter values representing k_1 , k_2 , and k_3 , respectively (Table 2 equations). Permeabilities of H_2O_2 and O_2 were obtained from the literature and assigned as 290 and 2 s^{-1} , respectively [27,28] The normalized value for γ H2AX was used in the logistic regression to measure how well the model viability could recapitulate the γ H2AX data. At the end of each simulation, the viability of each cell was gathered as a vector of binary values. For the ABM to appropriately model viability, the outputs of individual cell viabilities should fit a logistic regression model to the γ H2AX values, with “dead” simulated cells having higher levels of γ H2AX and “live” simulated cells having lower levels of γ H2AX. The *sklearn.linear_model.LogisticRegression* module was used with L2 norm penalty and a random_state seed of 0. The *sklearn.linear_model.LinearRegression* module was used to measure bulk correlation between simulation viability and γ H2AX averages per tumorsphere.

5.3 Results

5.3.1 Logic of agent-based models

We developed two agent-based models to represent the consumption of O_2 and the production of H_2O_2 within a cancer system. The first was a relatively simple model that simply converted O_2 into H_2O_2 implicitly including the NQO1 cycling reaction and antioxidant reactions within the cell. At each timestep, the concentration of H_2O_2 nearest each cell was used in equation 2 to determine a probability that the cell would die, Figure 9a. The second ABM used was more complex in that it included 3 reactions: one to

collectively represent the drug metabolism and production of H_2O_2 via NQO1, cytochrome p450 reductase, and superoxide dismutase 1, one to collectively represent the decomposition of H_2O_2 via antioxidant pathways such as peroxiredoxins, glutathione peroxidase/glutaredoxin, and catalase, and one to represent the reduction of $NADP^+$ into NADPH that would occur through numerous redox reactions in the cell. Using the same death probability equation, intracellular H_2O_2 was used to determine whether a cell would die or not, Figure 9b. The extracellular concentration grids for O_2 and H_2O_2 were solved with diffusion using equation 1 to determine the timestep of the numerical method. The logic of each ABM and order in which the multiple steps occurred is shown in Figure 9c.

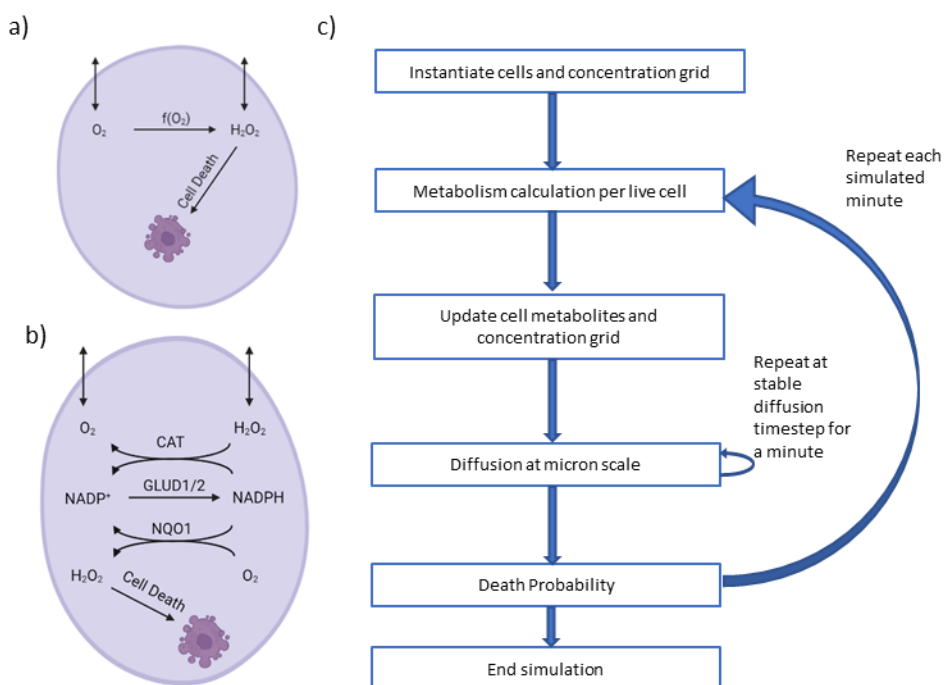


Figure 9: Agent-based model for β -lapachone metabolism. A) The intracellular metabolic model for the simple ABM (made with BioRender). B) The intracellular metabolic model for the complex ABM (made with BioRender). C) The logical flow of each ABM simulation.

5.3.2 Simple agent-based model highlights architectural effects on H₂O₂ production and cell death

The simple ABM was used with 4 different architectures: concentric NQO1⁺ with a core of NQO1⁺ cells and a surrounding ring of NQO1⁻ cells, concentric NQO1⁻ with a core of NQO1⁻ cells and a surrounding ring of NQO1⁺ cells, a salt-and-pepper “mixed” configuration, and two joined hemispheres denoted as “split” (Figure 10). While maintaining the same number of total cells in each simulation, the concentric NQO1⁺ architecture consisted of 300 NQO1⁺ cells in the center and 300 NQO1⁻ cells on the edge. The concentric NQO1⁻ architecture had NQO1⁻ cells in the center and NQO1⁺ on the edge. We varied the unknown model parameter for death “threshold” (equation 3) between 100 and 300 μM H₂O₂ in 50 μM increments. We show that the NQO1⁺ cells’ viability increases as the death threshold is raised; the differences among architectures is most notable at the moderate death threshold of 200 μM H₂O₂ (Figure 10a). The NQO1⁻ cells’ viability is generally high with higher death thresholds, but at lower death thresholds, the mixed and NQO1⁻ concentric architectures led to lower viabilities due to a bystander effect (orange and green boxes in Figure 10b). Following these results, we found that this could partially be explained by the number of NQO1⁺ neighbors surrounding NQO1⁻ cells. The mixed architecture led to the lowest NQO1⁻ viability, and the architecture with a core of NQO1⁻ cells had a lower viability than the NQO1⁺ center (Figure 10c). An example of the NQO1⁻ concentric architecture, Figure 10d–f represents snapshots of the simulation at 0, 60, and 120 minutes with the low death threshold of 100 μM H₂O₂.

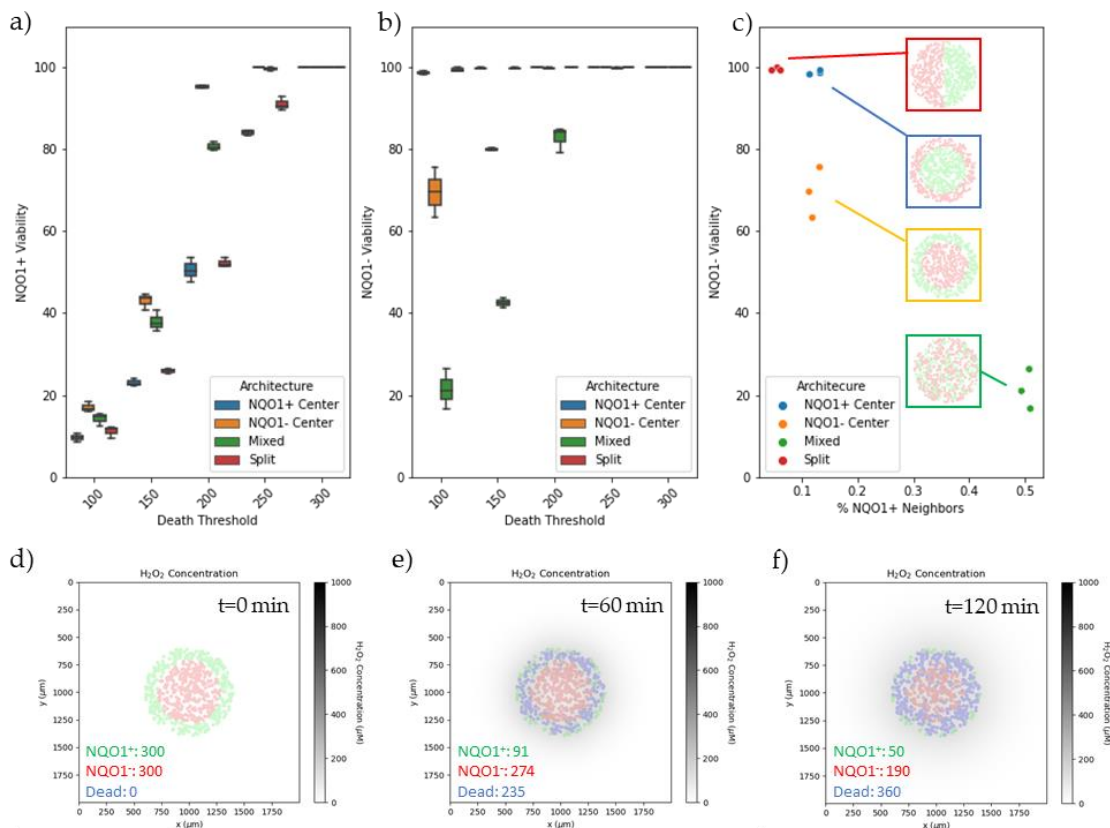


Figure 10: Simple ABM results show impact of architecture and death threshold on cell type viability.

A) NQO1⁺ cell viability at various death thresholds for different model architectures. B) NQO1⁻ cell viability at various death thresholds for different model architectures. Boxes represent interquartile range, the line within each box is the median value, and whiskers show minimum and maximum values from simulations. C) NQO1⁻ cell viability for each architecture based on % NQO1⁺ neighbors. NQO1⁻ center ABM example at 0 minutes (D), 60 minutes (E), and 120 minutes (F).

5.3.3 Mixed tumorsphere imaging and quantified protein expression analysis

To explore the effect of heterogeneity of drug within an engineered culture system that mimics the “mixed” architecture simulated in Figure 10, we grew tumorspheres with defined ratios of cell types for two days then treated with β -lapachone for two hours before being fixed and frozen. rSCC and SCC cell lines were used for creating the salt-and-pepper properties to reflect features of subclonal refractory populations that may occur in patient tumors; the rSCC cells were generated from the SCC parental line by repeated rounds of

ionizing radiation [24]. rSCCs have been reported to have over two times the amount of NQO1 mRNA than SCCs, and rSCCs have a β -lapachone IC_{50} of 3 μ M while SCCs are insensitive to β -lapachone [29]. We imaged the tumorspheres for CellTracker Red stained rSCC cells (Figure 11a), NQO1 and catalase (Figure 11b), and GLUD1/2 and γ H2AX (Figure 11c). After aligning the images, we segmented the cells within each image (Figure 11d) for quantification of protein expression levels in the individually identified cells. After processing the images and collecting the data, we standardized protein intensity values and γ H2AX levels to be between 0 and 1 and plotted them together and observed a slight trend with increasing NQO1 and GLUD1/2 expression leading to increasing γ H2AX intensity (Figure 11e). NQO1, catalase, GLUD1/2, and γ H2AX values per cell did not show a

relationship with the distance of cell location from the center of the tumorspheres
(Appendix Figure 13).

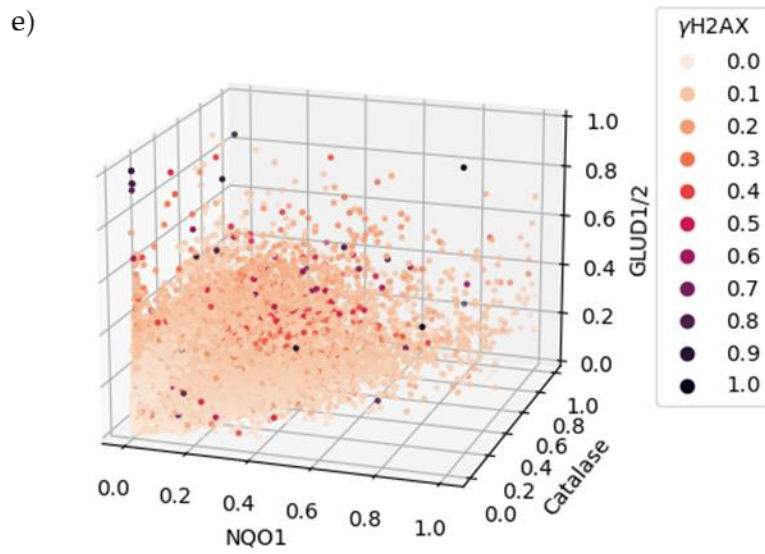
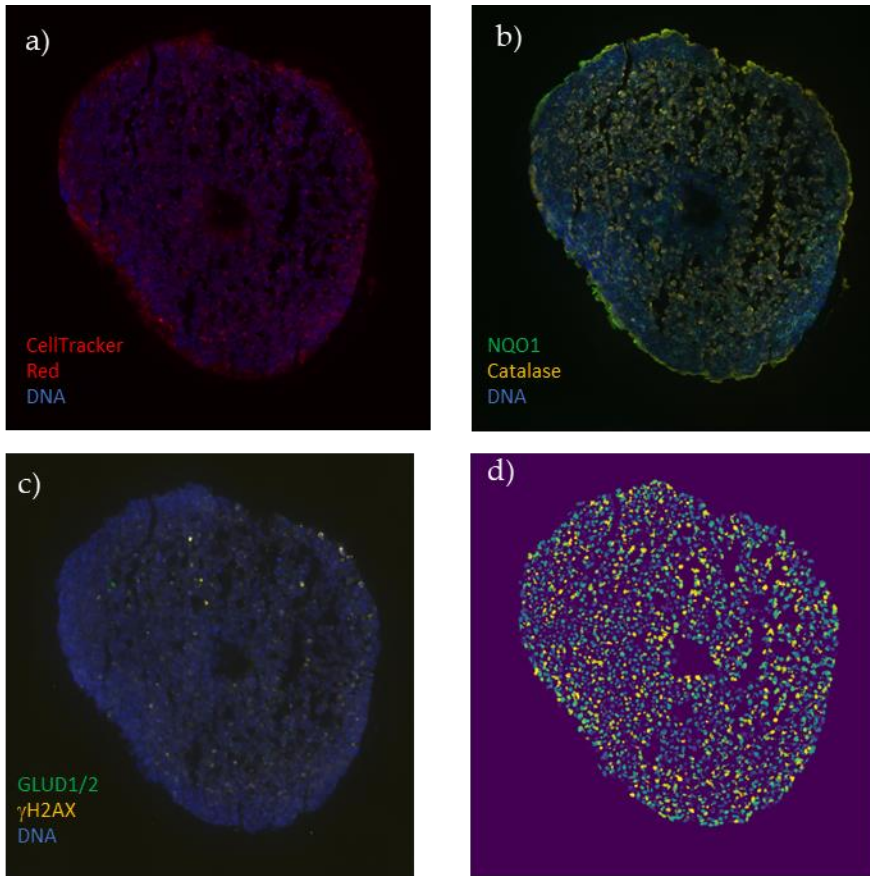


Figure 11: Cyclic immunofluorescence and single cell expression quantification.

A-C) Three cycles of CycIF results for a mixed tumorsphere with 90% rSCC cells and 10% SCC cells. D) Cells identified based on cycle 1 DNA staining. E) 3D scatter plot of NQO1, catalase, and GLUD1/2 intensities with marker colored by γ H2AX values using data from all tumorspheres listed in Table 3.

5.3.4 Parameterization of complex agent-based model

We ran simulations with the complex agent-based model from Figure 1b described in the methods section by deriving individual cellular parameters from the tumorsphere data. CycIF imaging data were quantified to determine the rate constants of each of the three reactions in the intracellular ODE model. With a ground truth based on γ H2AX immunofluorescent values, we scanned the parameter space across 2 death thresholds, 50 and 75 μ M, and 5 hill coefficients, 1, 2, 3, 5, and 10. After simulations were run for four tumorspheres that were 50% rSCC cells and 50% SCC cells and two tumorspheres that were 100% rSCC cells, the output viabilities were compared with each cell's γ H2AX value. A linear regression model measured the quality of a model fit for a specific death threshold and hill coefficient combination and resulted in a ideal threshold of 50 μ M and hill coefficient of 1. The pair of parameters that led to the highest average accuracy across all 6 training models was used to assess its accuracy on 4 testing models that had not been simulated yet. Using this 50 μ M threshold and hill coefficient of 1, the data from the remaining four tumorspheres were used to predict the potency of β -lapachone treatment under new conditions.

5.3.5 Complex ABM analysis

With the complex ABM death parameter fitted based on the γ H2AX data, we were able to analyze the impact of rSCC percentage on the simulation results. From plotting the simulation viabilities over time we observed that in the simulations with 100% rSCC, viability was surprisingly higher than simulations with fewer % rSCC cells. For the

tumorspheres with 90% rSCC, viability rapidly dropped off in less than 40 minutes of simulated time (Figure 12a). The 50% rSCC models showed large variability in viability. The two 75% rSCC tumorsphere models showed viability lower than the average 50% rSCC model and above the average 90% rSCC model (Figure 12a). There was a slight correlation between average γ H2AX intensity per tumorsphere and end viability of the simulation. An example of one of the tumorspheres with a death threshold of 50 μ M and hill coefficient of 3 is shown at 0, 60, and 120 minutes of the simulation (Figure 12c–e).

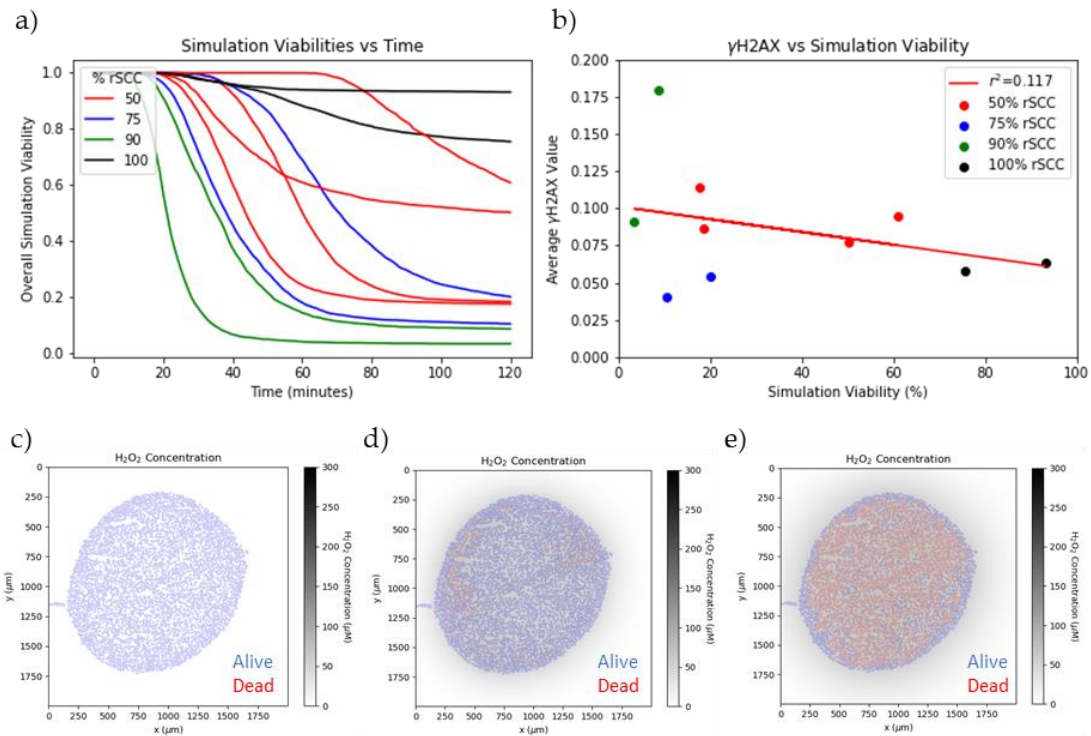


Figure 12: Complex ABM viability results show viability dependence on rSCC percentage. A) Viability of each tumorsphere simulation over time. Red/black lines represent fitted data and green/blue lines represent conditions reserved for validation under new experimental conditions. B) Correlation of γ H2AX and end viabilities for tumorsphere with markers colored by rSCC percentage. C-E) Example 50% complex tumorsphere ABM simulation at 0 minutes (C), 60 minutes (D), and 120 minutes (E).

5.4 Discussion

The impact that tumor heterogeneity, a known property of cancers, has on tumor metabolism of oxygen-utilizing drugs such as β -lapachone is currently underexplored. One challenge in interpreting drug potency in spatially complex tumors is the poorly understood “bystander effect”, which is seen when damaging byproducts (such as H_2O_2) from cells metabolizing drugs can diffuse outward to neighboring cells that do not metabolize drugs well. Tumor heterogeneity can result from vascularization, proliferation of subclonal populations as advantageous mutations accumulate, the nature of the cancer type, and/or anatomical location; these variations are hypothesized to lead to variable levels of bystander effects due to metabolically active cells yielding local differences in metabolism and nutrient concentrations.

Agent-based models are valuable tools for exploring how spatial variables can impact cell growth, drug treatments, and cell patterning among other outcomes [17,30–32]. To explore the impact that tumor heterogeneity could have specifically on β -lapachone potency, we constructed and simulated agent-based models that included diffusion across different multicellular organizational configurations and coupled intracellular reactions that describe major components of transport and ROS generation. Furthermore, we initialized our spatial models with parameters derived from quantified imaging data that established the heterogeneity of protein abundance in representative redox enzymes within cultured cancer cell line spheroids. Imaging data has been utilized in recent work by Cess and Finley to robustly estimate ABM parameters with representation learning [33], and additional methods to improve ABM parameterization are crucial to advancing this agent-

based modeling approach. Our engineered culture models treated with β -lapachone were used to test the accuracy of the computational simulations.

The bystander effect has been reported in recent years in the context of β -lapachone treatment, but the bystander effect in heterogeneous cancer systems is poorly understood [20]. Two approaches towards testing features of spatial organization led to insight in which properties were most susceptible to bystander effects of the β -lapachone. With the simple ABM, binary representation of NQO1 expression status was used to explore architecture properties. Our findings could be distilled down to the extent of proximal regions; the higher the number of NQO1⁺ cells there were near NQO1⁻ cells, the lower the NQO1⁻ viability. Interestingly, the NQO1⁺ core architecture led to a much higher NQO1⁻ viability than the NQO1⁻ core architecture. This observation can be explained by the fact that when NQO1⁺ cells are on the periphery of the system, the H₂O₂ they produced diffuses inward to the NQO1⁻ cells to lower the core cells' viability. In contrast, the NQO1⁺ center architecture leads to lower NQO1⁺ viability, but NQO1⁻ cells remain highly viable. We postulate that this outcome occurs due to the NQO1⁺ cells generating H₂O₂ rapidly, dying rapidly, and not remaining alive long enough to produce enough H₂O₂ to impact neighboring NQO1⁻ cells.

In the complex ABMs, we found that the tumorspheres with a higher percentage of rSCC cells had lower viabilities, but our conclusions are limited in that experimentally gathered γ H2AX values representing DNA damage may not be the best surrogate marker of eventual cell death caused by β -lapachone treatment. We established that radial distance did not correlate with NQO1 levels in our 50% rSCC spheroids (Appendix Figure 13), suggesting that O₂ tension was not playing a role in the enzyme expressions relevant to our

model system. Nonetheless, our finding of core NQO1⁺ cells not impacting the surrounding tumor tissue has relevance in possibly limiting bystander effects (and thus overall drug potency) in patients. Instead of generating an amplification of quinone cycling potency by accumulated H₂O₂ diffusing into the peripheral regions, cell death may be limited only to localized pockets of NQO1^{high} cells.

Due to the fact that the parameterization of the death threshold with the γ H2AX data could be improved further, we point to several limitations of our modeling approach. One addition that could be made is to experimentally determine the expression of additional proteins that are involved in the decomposition of H₂O₂ and additional cell death markers. Previous work regarding the impact of H₂O₂ on cell viability has considered low micromolar concentrations of H₂O₂ and the production of high H₂O₂ concentrations in the hundreds of micromolar are less well understood besides specific work with β -lapachone indicating programmed necrosis as the mechanism of death [20,34,35]. While γ H2AX is a marker of DNA damage, alternative signs of DNA damage could be probed such as hyperactivation of poly(ADP-ribose) polymerase-1 (PARP). PARP hyperactivation has been shown to occur after treatment with β -lapachone [19,36–38]; this could prove to be a more valuable cell death marker with which to validate the ABM. Additionally, quantification of NQO1, catalase, and GLUD1/2 values per cell as input data may not be a comprehensive set to determine how each cell will metabolize the drug and handle the damaging H₂O₂ product. The NQO1:catalase ratio has been debated as a useful metric for determining the efficacy of β -lapachone in cancer which we explored in a study analyzing and developing ODE models with single cell HNSCC data [21]. We found that in addition to NQO1 and antioxidant expression levels, NADPH-producing enzyme levels such as

GLUD1 and G6PD were predictive in β -lapachone outcomes. The importance of NADPH-producing enzymes has also been highlighted in the context β -lapachone treatment in HNSCC. Lewis et al. reported with flux balance analysis modeling that NADPH production can be rerouted through a number of different enzymes depending on the enzyme expression profile [29]. Variable metabolic rerouting would indicate that probing for additional NADPH enzymes prior to generating the ABM would provide a more comprehensive characterization of cellular NADPH-producing capacity to improve the ABMs.

Once properly expanded to better model the cell death within the model, this ABM can be utilized to determine how patient tumors would respond to β -lapachone. With excised tumors, sections can be made to collect expression of proteins to initialize the model. Then the production of H_2O_2 can be simulated to theorize how various spatial protein expression would impact β -lapachone treatment. A major difference between *in vitro* tumorspheres and real tumors is that real tumors are vascularized. Rather than being oxygen diffusion limited, the oxygen tension in tumors is more heterogeneous depending on the location of blood vessels in the tumor. Olsen and Siegelmann developed an agent-based model to simulate angiogenesis in tumors which is the formation of new blood vessels. In their study, models with angiogenesis did not always lead to lower hypoxic cell counts than models without angiogenesis that had a grid-like initial vasculature [31]. More recently, Rocha et al. in 2021 found that using ABMs could predict the formation of post-hypoxic plumes that arise in tumors due to post-hypoxic cells becoming more invasive and migrating toward oxygenated regions [39]. In tumors undergoing angiogenesis, pockets of low oxygen will occur in non-vascularized regions and pockets with high oxygen will arise

near vessels, resulting in a complex oxygen profile. More sophisticated whole-mount imaging methods such as light sheet confocal microscopy with immunofluorescence staining for endothelial markers such as CD31 would help initialize 3D modeling and yield experimental analysis for drug metabolism throughout the tumor and with more realistic behavior than the models presented here.

In conclusion, this research demonstrates the importance of using single cell data in spatial contexts, and how multicellular computational models can be used to understand cellular heterogeneity and organization on β -lapachone metabolism in HNSCC tumorspheres. Strategies that rely on bystander effects to amplify drug potency may have limited success depending on the spatial distribution of drug-metabolizing cells within the tumor tissue. With the complex nature of cancer, using experiments to gather single cell data and computationally modeling drug treatments will continue to improve the scientific community's ability to diagnose and treat cancers in the future.

CHAPTER 6 CONCLUSIONS AND FUTURE WORK

6.1 Conclusions

This project aimed to better understand the redox biology of HNSCC in the context of ROS-generating chemotherapies and to produce a useful model for predicting treatment efficacy given phenotype data. This was done by first assessing intracellular molecular profiles of HNSCC cells and how those profiles influence the production of H_2O_2 , the main cytotoxic product of these drugs. Second, the effect of perturbations of antioxidant enzymes and gap junctions involved in the resistance of β -lapachone on the potency of β -lapachone was assessed. Lastly, a model was synthesized using tumorsphere antioxidant spatial expression, and modeling results were compared to experimental γ H2AX levels to understand the predictive capacity of the model with spatial antioxidant expression as input.

The ODE modeling demonstrated the potential to identify relative importance of antioxidant enzymes in HNSCC and the response of a tumor to β -lapachone. Using scRNA-seq data to develop the enzymatic model of ROS generation and clearance, we found that NQO1:CAT is not the only metric to be considered when attempting to predict the response of a HNSCC tumor to β -lapachone. Other metrics such as expression of TXNRD1, POR, and NADPH-producing enzymes G6PD and GLUD1 have value in determining how a HNSCC tumor will respond to β -lapachone.

The perturbation studies on the effects of β -lapachone in general showed little effect on sensitization of the cell lines to β -lapachone. When using the stable NQO1 knockdown cell line we did see a dependence of H_2O_2 production on the proportion of knockdown cells used. However, the transient siRNA knockdowns of various antioxidant

enzymes did not lead to significant changes in H₂O₂ produced over 2 hours. While we did test for knockdown efficiency of NQO1, the transient nature of siRNA and the greater potential for off-target effects when using siRNA could have been a cause for these differences in silencing methods.

The results from the various ABM simulations highlighted the influence of spatial variables such as cell-type architecture and protein expression on the buildup of H₂O₂ within tumorspheres. We found with our “simple” ABM that specific architectures of drug-metabolizing cells in combination with non drug-metabolizing cells leads to differences in the bystander effect based on the proportion of neighboring cells that can metabolize the drug or not. Well-mixed architectures lead to lower viabilities overall in non drug-metabolizing cells, while the split and concentric architectures had higher viabilities of non drug-metabolizing cells due to pockets of non drug-metabolizing cells within the system that are protected from the drug-metabolizing cells. We found with our “complex” ABM that while the overall viabilities of the simulations matched what we expected based on the amount of NQO1^{high} cells within the experimental set up and microscopy images, we were unable to successfully match single cell simulation outcomes based on γ H2AX signal. The “complex” ABM also demonstrated proof of the concept that experimental CycIF results can be used to initialize ABM models and glean how well β -lapachone would be metabolized within a tumorsphere based on images of key proteins catalase, NQO1, and GLUD1/2.

Ultimately, this project lies at the overlap of many different fields of research. It contains redox biology, computational biology, oncology, and even machine learning. It can be difficult to piece together and utilize knowledge from these different areas to build

upon the scientific literature and make a contribution to the field, but it is undoubtedly unique in doing so. Combining both experimental and computational methods in a single thesis adds another layer of complexity but provides a researcher with a plethora of tools at their disposal.

6.2 Future Work

There are many avenues to go down when future researchers expand upon this work. This project provides a solid foundation for those interested in drug metabolism in cancer cells, in the effects of hypoxia and multicellular architecture on metabolism, and in how computational modeling can be used to inform us about situations experimentally infeasible. Here, I discuss in detail the potential routes that a new PhD student could take when approaching this subject of research.

6.2.1 Expansion of intracellular ODE model

While the development of the intracellular ODE model for this project included the assumed appropriate set of antioxidant enzymes, genome-scale metabolism models are becoming more popular (110,112,149). These genome-scale models typically utilize steady state assumptions to make up for a lack of computational power to dynamically represent the systems, but with increasing computational capabilities there is potential to include more terms and species in dynamic models in future research to analyze a more complete set of reactions.

Specifically regarding redox reactions within the cell, mitochondrial antioxidant enzymes were excluded in our model due to the cytosolic action of β -lapachone. It is well documented that much of a cell's ROS production takes place in the mitochondria and it is

estimated of 1% of the total oxygen consumed is converted into superoxide (150). It has also been shown that ROS produced there by complex III can be transferred to the cytosol, so the inclusion of mitochondrial enzymes in the model could more accurately represent the redox state of a cancer cell (151).

6.2.2 Characterization and modeling of patient tumor samples

Using tumor spheroids has its advantages such as being convenient for labs that do not have access to clinical collaborators, but taking tumor samples from HNSCC patients would undoubtedly have more biological value. Patient tumors are diverse and include stromal cells and immune cells which are increasingly becoming of interest in the cancer biology field due to their interactions with cancer cells and impact on treatment (152,153).

With advances in spatial characterization techniques that can quantify a high number of targets such as spatial transcriptomics or cyclic immunofluorescence, the ABM developed here could be used to model drug metabolism in patient tumors (154). Including immune cells and their interactions with cancer cells in the ABM using the spatial information gained with these new techniques would aid scientists developing immune-based therapies. If samples could be acquired in a clinical drug trial setting, the ABM could be further validated in the context of drug outcomes and point to potential biological or spatial characteristics of a tumor that are hindering the success of a drug. Further, with the full transcriptome resulting from a spatial transcriptomics experiment, genome-scale models could be implemented. These typically do not take spatial information into account, and if these comprehensive metabolic models were included in diffusion-based models such as ABMs, the value of their output would increase.

In the context of modeling oxygen tension and drug distribution within tumors and developing a more accurate representation, identifying where vasculature is located in a patient tumor sample is crucial. Because we used tumor spheroids, the only oxygen and drug interface was at the edge of the spheroid, but real tumors have complicated vasculature networks (16). This affects oxygen tension within a tumor, giving rise to pockets of hypoxia and normoxia. It also affects how well a drug will be distributed within a tumor (155). Building a patient tumor ABM would ideally have experimental information on a vasculature marker such as platelet and endothelial cell adhesion molecule 1 (PECAM1) so that the drug and oxygen distributions can be more accurately modeled.

6.2.3 Improved *in vitro* 3D models

Considering the difficulty of growing spheroids in suspension using ultra-low attachment plates, including extracellular matrix scaffolding would not only allow the cells to adhere to something other than neighboring cells, but the overall modeled tumor microenvironment would be more similar to *in vivo* tumors. There is also potential to include blood vessel cells in these experimental 3D models similar to the modeling work above. This could lead to understanding the effects of vasculature structure on drug and oxygen distributions and allow ABMs to be more easily validated than if they were to need patient tumors for validation.

6.3 Summary

In conclusion, we were able to generate several computational models of different scales that were specific to either single cells or cell lines, and combine them to better understand how redox biology, β -lapachone metabolism, and heterogeneity are connected.

We found that using single cell redox metabolism models from transcriptomic data can inform us on the potential of using β -lapachone in patients depending on their redox protein expression profiles. These models also pointed us towards specific redox enzymes other than NQO1 that should be focused on when determining eligibility of a patient for β -lapachone treatment. Additionally, experiments using tumor spheroids demonstrated relationships between antioxidant enzymes NQO1, catalase, and GLUD1/2, and DNA damage marker γ H2AX under β -lapachone treatment. Finally, we showed how this experimental cellular enzyme expression information and intracellular metabolic modeling can be used to develop an ABM that can predict ROS and oxygen levels within a spheroid.

Our findings highlight the value of using computational models to expand what we can glean from experiments, and while there are potential additions and improvements that can be made to both these modeling and experimental techniques, we presented novel findings with respect to β -lapachone metabolism in HNSCC.

APPENDIX

A.1. Chapter 3 Appendix

Table 3: Parameter Adjustments

Parameter	Unit	Average Value	Minimum Value	Maximum Value	Rate Law
k ₁	cm/s	2.00E-04	1.30E-07	4.80E-03	Fick's First Law
k ₂	μM/s	4.00E+00	n/a	n/a	Constant
k ₃	1/μM-s	6.00E+01	n/a	n/a	Mass Action
k ₄	1/μM-s	4.00E-02	n/a	n/a	Mass Action
k ₅	1/μM-s	1.00E+01	n/a	n/a	Mass Action
k ₆	1/μM-s	3.40E+01	n/a	n/a	Mass Action
k ₇	μM	5.70E+01	n/a	n/a	Michaelis-Menten
k ₈	1/μM-s	4.00E+01	n/a	n/a	Mass Action
k ₉	1/μM-s	7.20E-02	n/a	n/a	Mass Action
k ₁₀	1/s	3.00E-03	n/a	n/a	Mass Action
k ₁₁	1/s	1.50E+01	n/a	n/a	Mass Action
k ₁₂	1/μM-s	2.10E+00	n/a	n/a	Mass Action
k ₁₃	1/s	7.40E-05	n/a	n/a	Mass Action
k ₁₄	1/μM-s	1.00E-02	n/a	n/a	Mass Action
k ₁₅	1/μM-s	1.20E-01	n/a	n/a	Mass Action
k ₁₆	1/μM-s	9.10E-02	n/a	n/a	Mass Action
k ₁₇	1/μM-s	3.70E-02	n/a	n/a	Mass Action
k ₁₈	1/μM-s	5.00E-01	n/a	n/a	Mass Action
k ₁₉	1/μM-s	1.00E-01	n/a	n/a	Mass Action
k ₂₀	1/μM-s	3.20E+00	2.51E-02	7.31E+01	Mass Action
k ₂₁	1/μM-s	2.00E+01	1.23E-01	2.33E+02	Mass Action
k ₂₂	μM/s	3.75E+02	2.49E+00	5.02E+03	Michaelis-Menten
k ₂₃	cm/s	3.00E-03	n/a	n/a	Fick's First Law
k ₂₄	μM/s	4.10E-01	4.49E-03	8.64E+00	Constant
k ₂₅	μM/s	1.20E-02	n/a	n/a	Constant

k ₂₆	μM/s	1.20E-01	n/a	n/a	Mass Action
k ₂₇	μM/s	7.45E-04	n/a	n/a	Mass Action
k ₂₈	μM/s	6.97E-04	n/a	n/a	Constant
k ₂₉	1/μM-s	1.62E+02	6.78E-01	1.17E+03	Mass Action
k ₃₀	1/μM-s	3.00E+02	n/a	n/a	Mass Action
k ₃₁	1/μM-s	3.00E+02	n/a	n/a	Mass Action
k ₃₂	1/μM-s	6.40E+03	1.64E+01	2.52E+04	Mass Action
k ₃₃	1/μM-s	1.20E-02	5.93E-05	1.04E-01	Mass Action
k ₃₄	cm/s	1.00E-06	n/a	n/a	Fick's First Law
k ₃₅	1/μM-s	5.00E-02	8.81E-05	1.91E-01	Mass Action
k ₃₆	cm/s	1.00E-06	n/a	n/a	Fick's First Law

Parameter	Type	Reaction Stoichiometry	scRNA-seq Adjustment
k ₁	P	H ₂ O ₂ ^c <-> H ₂ O ₂ ^e	AQP3 % deviation from mean
k ₂	n/a	-> H ₂ O ₂ ^c	n/a
k ₃	k _{cat}	H ₂ O ₂ ^c +GPX1r -> GPX1o	n/a
k ₄	k _{cat}	GPX1o + GSH -> GPX1-SG	n/a
k ₅	k _{cat}	GPX1-SG + GSH -> GPX1r + GSSG	n/a
k ₆	k _{cat}	H ₂ O ₂ ^x ->	n/a
k ₇	K _m	NADP ⁺ -> NADPH	n/a
k ₈	k _{cat}	Prx1/2-SH + H ₂ O ₂ ^c -> Prx1/2-SOH	n/a
k ₉	k _{cat}	Prx1/2-SOH + H ₂ O ₂ ^c -> Prx1/2-SOOH	n/a
k ₁₀	k _{cat}	Prx1/2-SOOH -> Prx1/2-SOH	n/a
k ₁₁	k _{cat}	Prx1/2-SOH -> Prx1/2-SS	n/a
k ₁₂	k _{cat}	Prx1/2-SS + Trx1-SH -> Prx1/2-SH + Trx1-SS	n/a
k ₁₃	k _{cat}	2GSH -> GSSG	n/a
k ₁₄	k _{cat}	Pr-SH + H ₂ O ₂ ^c -> Pr-SOH	n/a
k ₁₅	k _{cat}	Pr-SOH + GSH -> Pr-SSG	n/a
k ₁₆	k _{cat}	Pr-SSG + Grx-SH -> Grx-SSG + Pr-SH	n/a

k ₁₇	k _{cat}	Grx-SSG + GSH -> Grx-SH + GSSG	n/a
k ₁₈	k _{cat}	Pr-(SH) ₂ + H ₂ O ₂ ^c -> Pr-SS	n/a
k ₁₉	k _{cat}	Pr-SS + Trx-SH -> Pr-SH + Trx-SS	n/a
k ₂₀	k _{cat}	NADPH + GSSG -> 2GSH + NADP ⁺	GSR % deviation from mean
k ₂₁	k _{cat}	Trx-SS + NADPH -> Trx-SH + NADP ⁺	TXNRD1 % deviation from mean
k ₂₂	k _{cat}	NADP ⁺ -> NADPH	G6PD and GLUD1 % deviation from mean
k ₂₃	P	H ₂ O ₂ ^x <-> H ₂ O ₂ ^c	n/a
k ₂₄	n/a	-> GSH	GCLC % deviation from mean
k ₂₅	n/a	GSSG ->	n/a
k ₂₆	k _{cat}	GSSG + GSH ->	n/a
k ₂₇	k _{cat}	Trx-SH ->	n/a
k ₂₈	n/a	-> Trx-SH	n/a
k ₂₉	k _{cat}	β-lapQ ^c + NADPH -> β-lapHQ + NADP ⁺	NQO1 % deviation from mean
k ₃₀	k _{cat}	β-lapHQ + O ₂ -> β-lapSQ + O ₂ [*]	n/a
k ₃₁	k _{cat}	β-lapSQ + O ₂ -> β-lapQ ^c + O ₂ [*]	n/a
k ₃₂	k _{cat}	2O ₂ [*] -> H ₂ O ₂ + O ₂	SOD1 % deviation from mean
k ₃₃	k _{cat}	β-lapQ ^c + NADPH -> β-lapSQ + NADP ⁺ ; β-lapSQ + NADPH -> β-lapHQ + NADP ⁺	POR % deviation from mean
k ₃₄	P	β-lapQ ^c <-> β-lapQ ^e	n/a
k ₃₅	k _{cat}	β-lapHQ + GSH -> β-lapHQ-SG ^c	GSTP1 % deviation from mean
k ₃₆	P	β-lapHQ-SG ^c <-> β-lapHQ-SG ^e	n/a

Table 4: Initial Species Adjustments

Species Name	Average Initial Value (μM)	Minimum Value (μM)	Maximum Value (μM)	scRNA-seq Adjustment
H ₂ O ₂ ^e	0.00E+00	n/a	n/a	n/a
H ₂ O ₂ ^c	1.00E-03	n/a	n/a	n/a
GPX _r	5.04E-02	1.66E-04	2.48E-01	GPX1 abundance
GPX _o	1.01E-11	3.32E-14	4.96E-11	n/a
GPX-SG	1.01E-11	3.32E-14	4.96E-11	n/a
GSH	3.68E+02	n/a	n/a	n/a

GSSG	1.79E+00	n/a	n/a	n/a
CAT	9.57E-02	5.60E-04	1.39E+00	CAT abundance
H ₂ O ₂ ^x	1.00E-10	n/a	n/a	n/a
Prx1/2-SH	1.12E+01	2.79E-02	4.71E+01	PRDX1 and PRDX2 abundance
Prx1/2-SOH	5.83E-09	1.45E-11	2.45E-08	n/a
Prx1/2-SOOH	5.83E-09	1.45E-11	2.45E-08	n/a
Prx1/2-SS	5.60E-02	1.40E-04	2.36E-01	n/a
Trx-SH	1.13E+00	3.28E-03	4.75E+00	TXN abundance
Trx-SS	1.98E-01	5.75E-04	8.33E-01	n/a
Pr-SH	5.00E+01	n/a	n/a	n/a
Pr-SOH	2.50E-01	n/a	n/a	n/a
Pr-SSG	2.50E-01	n/a	n/a	n/a
Grx-SH	1.90E-01	7.10E-04	3.13E+00	GLRX1 abundance
Grx-SSG	9.50E-04	3.55E-06	1.57E-02	n/a
Pr-(SH) ₂	4.50E+02	n/a	n/a	n/a
Pr-SS	2.25E+00	n/a	n/a	n/a
NADPH	3.00E+01	n/a	n/a	n/a
NADP ⁺	3.00E-01	n/a	n/a	n/a
β-lapQ	0.00E+00	n/a	n/a	n/a
β-lapHQ	0.00E+00	n/a	n/a	n/a
β-lapSQ	0.00E+00	n/a	n/a	n/a
O ₂ ^{•-}	0.00E+00	n/a	n/a	n/a
O ₂	2.60E+02	n/a	n/a	n/a
β-lapQ ^e	3.00E+00	n/a	n/a	n/a
β-lapHQ-SG ^c	0.00E+00	n/a	n/a	n/a
β-lapHQ-SG ^e	0.00E+00	n/a	n/a	n/a

A.2. Chapter 5 Appendix

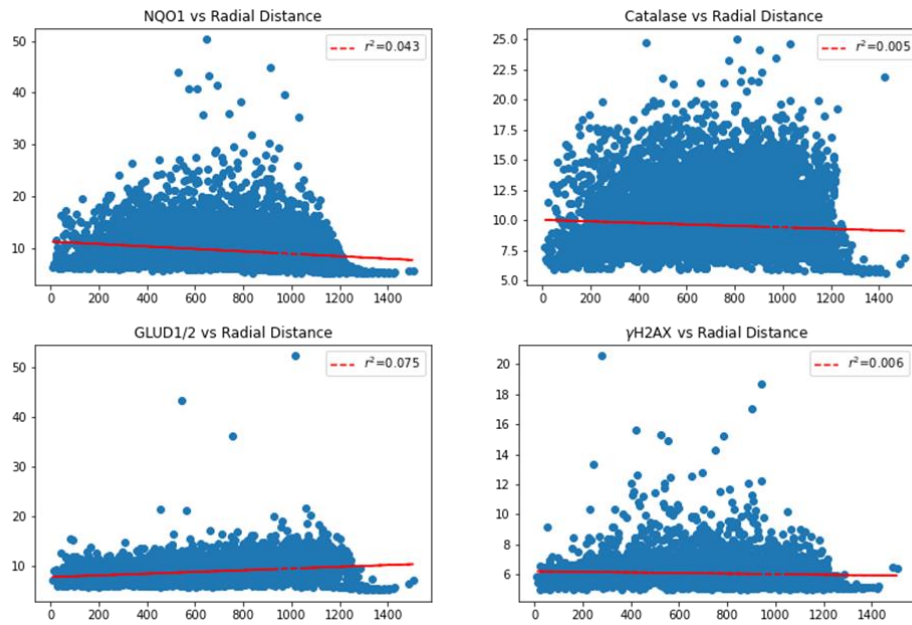


Figure 13: Correlations between protein intensity and distance from center of tumorsphere.

REFERENCES

1. Siegel RL, Miller KD, Fuchs HE, Jemal A. Cancer statistics, 2022. *CA Cancer J Clin* [Internet]. American Cancer Society; 2022 [cited 2022 Mar 16];72:7–33. Available from: <https://onlinelibrary.wiley.com/doi/full/10.3322/caac.21708>
2. Bose P, Brockton NT, Dort JC. Head and neck cancer: From anatomy to biology. *Int J Cancer*. 2013;133:2013–23.
3. Sawabe M, Ito H, Oze I, Hosono S, Kawakita D, Tanaka H, et al. Heterogeneous impact of alcohol consumption according to treatment method on survival in head and neck cancer: A prospective study. *Cancer Sci*. Blackwell Publishing Ltd; 2017;108:91–100.
4. Osazuwa-Peters N, Boakye EA, Chen BY, Tobo BB, Varvares MA. Association between head and neck squamous cell carcinoma survival, smoking at diagnosis, and marital status. *JAMA Otolaryngol Head Neck Surg*. American Medical Association; 2018;144:43–50.
5. Sturgis EM, Cinciripini PM. Trends in head and neck cancer incidence in relation to smoking prevalence: An emerging epidemic of human papillomavirus-associated cancers? *Cancer*. 2007. page 1429–35.
6. Rischin D, Young RJ, Fisher R, Fox SB, Le QT, Peters LJ, et al. Prognostic significance of p16INK4A and human papillomavirus in patients with oropharyngeal cancer treated on TROG 02.02 phase III trial. *Journal of Clinical Oncology*. 2010;28:4142–8.
7. Fakhry C, Westra WH, Li S, Cmelak A, Ridge JA, Pinto H, et al. Improved survival of patients with human papillomavirus-positive head and neck squamous cell carcinoma in a prospective clinical trial. *J Natl Cancer Inst*. 2008;100:261–9.
8. Kobayashi K, Hisamatsu K, Suzui N, Hara A, Tomita H, Miyazaki T. A Review of HPV-Related Head and Neck Cancer. *J Clin Med*. MDPI AG; 2018;7:241.

9. Lassen P. The role of Human papillomavirus in head and neck cancer and the impact on radiotherapy outcome. *Radiother Oncol* [Internet]. *Radiother Oncol*; 2010 [cited 2022 Sep 12];95:371–80. Available from: <https://pubmed.ncbi.nlm.nih.gov/20493569/>
10. Wegge M, Dok R, Nuyts S. Hypoxia and Its Influence on Radiotherapy Response of HPV-Positive and HPV-Negative Head and Neck Cancer. *Cancers (Basel)* [Internet]. Multidisciplinary Digital Publishing Institute (MDPI); 2021 [cited 2022 Sep 12];13. Available from: </pmc/articles/PMC8656584/>
11. Krupar R, Robold K, Gaag D, Spanier G, Kreutz M, Renner K, et al. Immunologic and metabolic characteristics of HPV-negative and HPV-positive head and neck squamous cell carcinomas are strikingly different. *Virchows Arch* [Internet]. Springer; 2014 [cited 2022 Nov 25];465:299–312. Available from: <https://link.springer.com/article/10.1007/s00428-014-1630-6>
12. Mroz EA, Tward AD, Pickering CR, Myers JN, Ferris RL, Rocco JW. High intratumor genetic heterogeneity is related to worse outcome in patients with head and neck squamous cell carcinoma. *Cancer* [Internet]. John Wiley & Sons, Ltd; 2013 [cited 2022 Nov 27];119:3034–42. Available from: <https://onlinelibrary.wiley.com/doi/full/10.1002/cncr.28150>
13. Li H, Wawrose JS, Gooding WE, Garraway LA, Lui VWY, Peyser ND, et al. Genomic analysis of head and neck squamous cell carcinoma cell lines and human tumors: A rational approach to preclinical model selection. *Molecular Cancer Research* [Internet]. American Association for Cancer Research Inc.; 2014 [cited 2022 Nov 27];12:571–82. Available from: <https://aacrjournals.org/mcr/article/12/4/571/89438/Genomic-Analysis-of-Head-and-Neck-Squamous-Cell>

14. Bredell MG, Ernst J, El-Kochairi I, Dahlem Y, Ikenberg K, Schumann DM. Current relevance of hypoxia in head and neck cancer. *Oncotarget*. Impact Journals LLC; 2016. page 50781–804.
15. Zhu G, Peng F, Gong W, She L, Wei M, Tan H, et al. Hypoxia promotes migration/invasion and glycolysis in head and neck squamous cell carcinoma via an HIF-1 α -MTDH loop. *Oncol Rep*. Spandidos Publications; 2017;38:2893–900.
16. Nagy JA, Chang S-H, Shih S-C, Dvorak AM, Dvorak HF. Heterogeneity of the Tumor Vasculature. 2010;
17. Baluk P, Hashizume H, McDonald DM. Cellular abnormalities of blood vessels as targets in cancer. *Curr Opin Genet Dev*. 2005. page 102–11.
18. Li JZ, Gao W, Chan JY-W, Ho W-K, Wong T-S. Hypoxia in Head and Neck Squamous Cell Carcinoma. *ISRN Otolaryngol*. Hindawi Limited; 2012;2012:1–8.
19. Nordsmark M, Overgaard M, Overgaard J. Pretreatment oxygenation predicts radiation response in advanced squamous cell carcinoma of the head and neck. *Radiotherapy and Oncology*. Elsevier Ireland Ltd; 1996;41:31–9.
20. Brizel DM, Sibley GS, Prosnitz LR, Scher RL, Dewhirst MW. Tumor hypoxia adversely affects the prognosis of carcinoma of the head and neck. *Int J Radiat Oncol Biol Phys*. 1997;38:285–9.
21. Chandel NS, Maltepe E, Goldwasser E, Mathieu CE, Simon MC, Schumacker PT. Mitochondrial reactive oxygen species trigger hypoxia-induced transcription. *Proc Natl Acad Sci U S A*. 1998;95:11715–20.
22. Bell EL, Klimova TA, Eisenbart J, Schumacker PT, Chandel NS. Mitochondrial Reactive Oxygen Species Trigger Hypoxia-Inducible Factor-Dependent Extension of the Replicative Life Span during Hypoxia. *Mol Cell Biol*. American Society for Microbiology; 2007;27:5737–45.

23. E P, P T-A, S S, L S. The NRF2/KEAP1 Axis in the Regulation of Tumor Metabolism: Mechanisms and Therapeutic Perspectives. *Biomolecules* [Internet]. 2020;10. Available from: <http://www.ncbi.nlm.nih.gov/pubmed/32443774>
24. Liou GY, Storz P. Reactive oxygen species in cancer. *Free Radic Res.* 2010. page 479–96.
25. Khavari TA, Rinn J. Ras/Erk MAPK signaling in epidermal homeostasis and neoplasia. *Cell Cycle.* Taylor and Francis Inc.; 2007. page 2928–31.
26. Roberts PJ, Der CJ. Targeting the Raf-MEK-ERK mitogen-activated protein kinase cascade for the treatment of cancer. *Oncogene.* 2007. page 3291–310.
27. Burdick AD, Davis JW, Liu KJ, Hudson LG, Shi H, Monske ML, et al. Benzo(a)pyrene Quinones Increase Cell Proliferation, Generate Reactive Oxygen Species, and Transactivate the Epidermal Growth Factor Receptor in Breast Epithelial Cells. *Cancer Res.* 2003;63:7825–33.
28. Wang Y, Huang X, Cang H, Gao F, Yamamoto T, Osaki T, et al. The endogenous reactive oxygen species promote NF- κ B activation by targeting on activation of NF- κ B-inducing kinase in oral squamous carcinoma cells. *Free Radic Res.* 2007;41:963–71.
29. Kirshner JR, He S, Balasubramanyam V, Kepros J, Yang CY, Zhang M, et al. Elesclomol induces cancer cell apoptosis through oxidative stress. *Mol Cancer Ther.* 2008;7:2319–27.
30. Pardee A, Li Y, Li C. Cancer Therapy with beta-Lapachone. *Curr Cancer Drug Targets.* Bentham Science Publishers Ltd.; 2005;2:227–42.
31. Lundberg AP, Francis JM, Pajak M, Parkinson EI, Wycislo KL, Rosol TJ, et al. Pharmacokinetics and derivation of an anticancer dosing regimen for the novel anti-cancer agent isobutyl-deoxyxyboquinone (IB-DNQ), a NQO1 bioactivatable molecule, in the domestic felid species. *Invest New Drugs.* Springer New York LLC; 2017;35:134–44.

32. Wondrak GT. Redox-directed cancer therapeutics: Molecular mechanisms and opportunities. *Antioxid Redox Signal*. 2009. page 3013–69.
33. Lyhne NM, Primdahl H, Kristensen CA, Andersen E, Johansen J, Andersen LJ, et al. The DAHANCA 6 randomized trial: Effect of 6 vs 5 weekly fractions of radiotherapy in patients with glottic squamous cell carcinoma. *Radiotherapy and Oncology*. Elsevier; 2015;117:91–8.
34. Johnson DE, Burtneß B, Leemans CR, Lui VWY, Bauman JE, Grandis JR. Head and neck squamous cell carcinoma. *Nature Reviews Disease Primers* 2020 6:1 [Internet]. Nature Publishing Group; 2020 [cited 2022 Nov 25];6:1–22. Available from: <https://www.nature.com/articles/s41572-020-00224-3>
35. Weinstein GS, O'Malley BW, Magnuson JS, Carroll WR, Olsen KD, Daio L, et al. Transoral robotic surgery: A multicenter study to assess feasibility, safety, and surgical margins. *Laryngoscope* [Internet]. John Wiley & Sons, Ltd; 2012 [cited 2022 Nov 21];122:1701–7. Available from: <https://onlinelibrary.wiley.com/doi/full/10.1002/lary.23294>
36. Bernier J, Dömenge C, Ozsahin M, Matuszewska K, Lefebvre J-L, Greiner RH, et al. Postoperative irradiation with or without concomitant chemotherapy for locally advanced head and neck cancer. *N Engl J Med* [Internet]. *N Engl J Med*; 2004 [cited 2022 Nov 25];350:1945–52. Available from: <https://pubmed.ncbi.nlm.nih.gov/15128894/>
37. Specenier P, Vermorken JB. Cetuximab: its unique place in head and neck cancer treatment. *Biologics* [Internet]. Dove Press; 2013 [cited 2022 Nov 21];7:77. Available from: </pmc/articles/PMC3665438/>
38. Burtneß B, Harrington KJ, Greil R, Soulières D, Tahara M, de Castro G, et al. Pembrolizumab alone or with chemotherapy versus cetuximab with chemotherapy for recurrent or metastatic squamous cell carcinoma of the head and neck

- (KEYNOTE-048): a randomised, open-label, phase 3 study. *The Lancet*. Lancet Publishing Group; 2019;394:1915–28.
39. Boothman DA, Greer S, Pardee AB. Potentiation of Halogenated Pyrimidine Radiosensitizers in Human Carcinoma Cells by β -Lapachone(3,4-Dihydro-2,2-dimethyl-2'-naphtho[1,2-b]pyran-5,6-dione), a Novel DNA Repair Inhibitor. *Cancer Res* [Internet]. 1987 [cited 2022 Nov 25];47:5361–6. Available from: <http://aacrjournals.org/cancerres/article-pdf/47/20/5361/2429386/cr0470205361.pdf>
 40. Pink JJ, Planchon SM, Tagliarino C, Varnes ME, Siegel D, Boothman DA. NAD(P)H:Quinone Oxidoreductase Activity Is the Principal Determinant of β -Lapachone Cytotoxicity. *Journal of Biological Chemistry* [Internet]. 2000;275:5416–24. Available from: <http://www.jbc.org/content/275/8/5416.abstract>
 41. Winterbourn CC. The biological chemistry of hydrogen peroxide. *Methods Enzymol* [Internet]. *Methods Enzymol*; 2013 [cited 2022 Nov 25];528:3–25. Available from: <https://pubmed.ncbi.nlm.nih.gov/23849856/>
 42. Torrente L, Prieto N, Falzone A, Boothman DA, Haura EB, DeNicola GM. Inhibition of TXNRD or SOD1 overcomes NRF2-mediated resistance to β -lapachone. *bioRxiv*. Cold Spring Harbor Laboratory; 2019;849927.
 43. Bey EA, Bentle MS, Reinicke KE, Dong Y, Yang CR, Girard L, et al. An NQO1- and PARP-1-mediated cell death pathway induced in non-small-cell lung cancer cells by β -lapachone. *Proc Natl Acad Sci U S A*. 2007;104:11832–7.
 44. Chakrabarti G, Moore ZR, Luo X, Ilcheva M, Ali A, Padanad M, et al. Targeting glutamine metabolism sensitizes pancreatic cancer to PARP-driven metabolic catastrophe induced by β -lapachone. *Cancer Metab* [Internet]. 2015 [cited 2019 Oct 28];3:12. Available from: <http://www.ncbi.nlm.nih.gov/pubmed/26462257>

45. Huang X, Dong Y, Bey EA, Kilgore JA, Bair JS, Li L-S, et al. An NQO1 Substrate with Potent Antitumor Activity That Selectively Kills by PARP1-Induced Programmed Necrosis. *Cancer Res* [Internet]. 2012;72:3038–47. Available from: <http://www.ncbi.nlm.nih.gov/pmc/articles/PMC4795165/>
46. Cao L, Li LS, Spruell C, Xiao L, Chakrabarti G, Bey EA, et al. Tumor-Selective, Futile Redox Cycle-Induced Bystander Effects Elicited by NQO1 Bioactivatable Radiosensitizing Drugs in Triple-Negative Breast Cancers. *Antioxid Redox Signal*. Mary Ann Liebert, Inc., publishers; 2014;21:237–50.
47. Bey EA, Reinicke KE, Srougi MC, Varnes M, Anderson V, Pink JJ, et al. Catalase abrogates β -lapachone-induced PARP1 hyperactivation-directed programmed necrosis in NQO1-positive breast cancers. *Mol Cancer Ther* [Internet]. 2013; Available from: <http://mct.aacrjournals.org/content/molcanther/early/2013/07/24/1535-7163.MCT-12-0962.full.pdf>
48. Dong Y, Chin S-F, Blanco E, Bey EA, Kabbani W, Xie X-J, et al. Intratumoral Delivery of β -Lapachone via Polymer Implants for Prostate Cancer Therapy. *Clinical Cancer Research*. 2009;15:131–9.
49. Cao L, Li LS, Spruell C, Xiao L, Chakrabarti G, Bey EA, et al. Tumor-selective, futile redox cycle-induced bystander effects elicited by NQO1 bioactivatable radiosensitizing drugs in triple-negative breast cancers. *Antioxid Redox Signal*. Mary Ann Liebert Inc.; 2014. page 237–50.
50. Torrente L, Prieto-Farigua N, Falzone A, Elkins CM, Boothman DA, Haura EB, et al. Inhibition of TXNRD or SOD1 overcomes NRF2-mediated resistance to β -lapachone. *Redox Biol*. Elsevier B.V.; 2020;30:101440.
51. Gerber DE, Beg MS, Fattah F, Frankel AE, Fatunde O, Arriaga Y, et al. Phase 1 study of ARQ 761, a β -lapachone analogue that promotes NQO1-mediated

- programmed cancer cell necrosis. *Br J Cancer*. Nature Publishing Group; 2018;119:928–36.
52. Griffith LG, Swartz MA. Capturing complex 3D tissue physiology in vitro. *Nat Rev Mol Cell Biol*. 2006. page 211–24.
 53. Suuronen EJ, Sheardown H, Newman KD, McLaughlin CR, Griffith M. Building in vitro models of organs. *Int Rev Cytol*. 2005. page 137–73.
 54. Sivaraman A, Leach J, Townsend S, Iida T, Hogan B, Stolz D, et al. A Microscale In Vitro Physiological Model of the Liver: Predictive Screens for Drug Metabolism and Enzyme Induction. *Curr Drug Metab*. Bentham Science Publishers Ltd.; 2005;6:569–91.
 55. Roskelley CD, Desprez PY, Bissell MJ. Extracellular matrix-dependent tissue-specific gene expression in mammary epithelial cells requires both physical and biochemical signal transduction. *Cell Biology*. 1994.
 56. Knight B, Laukaitis C, Akhtar N, Hotchin NA, Edlund M, Horwitz AR. Visualizing muscle cell migration in situ. *Current Biology*. Current Biology Ltd; 2000;10:576–85.
 57. Loessner D, Stok KS, Lutolf MP, Hutmacher DW, Clements JA, Rizzi SC. Bioengineered 3D platform to explore cell-ECM interactions and drug resistance of epithelial ovarian cancer cells. *Biomaterials*. 2010;31:8494–506.
 58. Song H, David O, Clejan S, Giordano CL, Pappas-Lebeau H, Xu L, et al. Spatial composition of prostate cancer spheroids in mixed and static cultures. *Tissue Eng*. 2004. page 1266–76.
 59. Li CL, Tian T, Nan KJ, Zhao N, Guo YH, Cui J, et al. Survival advantages of multicellular spheroids vs. monolayers of HepG2 cells in vitro. *Oncol Rep*. 2008;20:1465–71.

60. Ridky TW, Chow JM, Wong DJ, Khavari PA. Invasive three-dimensional organotypic neoplasia from multiple normal human epithelia. *Nat Med.* 2010;16:1450–6.
61. Ghosh S, Spagnoli GC, Martin I, Ploegert S, Demougin P, Heberer M, et al. Three-dimensional culture of melanoma cells profoundly affects gene expression profile: A high density oligonucleotide array study. *J Cell Physiol.* 2005;204:522–31.
62. Glinsky V V., Huflejt ME, Glinsky G V., Deutscher SL, Quinn TP. Effects of Thomsen-Friedenreich antigen-specific peptide P-30 on β -galactoside-mediated homotypic aggregation and adhesion to the endothelium of MDA-MB-435 human breast carcinoma cells. *Cancer Res.* 2000;60:2584–8.
63. Wu FJ, Friend JR, Hsiao CC, Zilliox MJ, Ko W-J, Cerra FB, et al. Efficient assembly of rat hepatocyte spheroids for tissue engineering applications. *Biotechnol Bioeng.* 1996;50:404–15.
64. Foty R. A simple hanging drop cell culture protocol for generation of 3D spheroids. *Journal of Visualized Experiments.* *Journal of Visualized Experiments*; 2011;
65. Koide N, Sakaguchi K, Koide Y, Asano K, Kawaguchi M, Matsushima H, et al. Formation of multicellular spheroids composed of adult rat hepatocytes in dishes with positively charged surfaces and under other nonadherent environments. *Exp Cell Res.* 1990;186:227–35.
66. Ziskin MC. Growth of Mammalian Multicellular Tumor Spheroids. *Cancer Res.* 1983;43:556–60.
67. Underhill GH, Chen AA, Albrecht DR, Bhatia SN. Assessment of hepatocellular function within PEG hydrogels. *Biomaterials.* 2007;28:256–70.
68. Wang C, Tang Z, Zhao Y, Yao R, Li L, Sun W. Three-dimensional in vitro cancer models: A short review. *Biofabrication.* Institute of Physics Publishing; 2014.

69. Lei KF, Wu MH, Hsu CW, Chen YD. Real-time and non-invasive impedimetric monitoring of cell proliferation and chemosensitivity in a perfusion 3D cell culture microfluidic chip. *Biosens Bioelectron.* Elsevier; 2014;51:16–21.
70. Jensen C, Teng Y. Is It Time to Start Transitioning From 2D to 3D Cell Culture? *Front Mol Biosci.* Frontiers Media S.A.; 2020;7:33.
71. Heiden MG, Cantley LC, Thompson CB. Understanding the Warburg Effect: The Metabolic Requirements of Cell Proliferation. *Science* [Internet]. NIH Public Access; 2009 [cited 2022 Nov 25];324:1029. Available from: </pmc/articles/PMC2849637/>
72. Sachs RK, Hlatky LR, Hahnfeldt P. Simple ODE models of tumor growth and anti-angiogenic or radiation treatment. *Math Comput Model.* 2001;33:1297–305.
73. Spencer SL, Berryman MJ, García JA, Abbott D. An ordinary differential equation model for the multistep transformation to cancer. *J Theor Biol.* 2004;231:515–24.
74. Resendis-Antonio O, González-Torres C, Jaime-Muñoz G, Hernandez-Patiño CE, Salgado-Muñoz CF. Modeling metabolism: A window toward a comprehensive interpretation of networks in cancer. *Semin Cancer Biol.* Academic Press; 2015. page 79–87.
75. Bachmann J, Raue A, Schilling M, Becker V, Timmer J, Klingmüller U. Predictive mathematical models of cancer signalling pathways. *J Intern Med.* 2012. page 155–65.
76. Itani S, Gray J, Tomlin CJ. An ODE model for the HER2/3-AKT signaling pathway in cancers that overexpress HER2. 2010. page 1235–41.
77. Misra P. *Ordinary Differential Equations in Cancer Biology.*
78. Finn NA, Findley HW, Kemp ML. A Switching Mechanism in Doxorubicin Bioactivation Can Be Exploited to Control Doxorubicin Toxicity. Lengauer T, editor. *PLoS Comput Biol.* 2011;7:e1002151.

79. Finn NA, Raddatz AD, Kemp ML. Systems Biology Approaches to Enzyme Kinetics. *Methods in Molecular Biology* [Internet]. Humana Press Inc.; 2021 [cited 2022 Nov 27];2342:419–40. Available from: https://link.springer.com/protocol/10.1007/978-1-0716-1554-6_15
80. McDougall SR, Anderson ARA, Chaplain MAJ, Sherratt JA. Mathematical modelling of flow through vascular networks: Implications for tumour-induced angiogenesis and chemotherapy strategies. *Bull Math Biol. Academic Press*; 2002;64:673–702.
81. Macklin P, Edgerton ME, Thompson AM, Cristini V. Patient-calibrated agent-based modelling of ductal carcinoma in situ (DCIS): From microscopic measurements to macroscopic predictions of clinical progression. *J Theor Biol.* 2012;301:122–40.
82. Anderson ARA, Rejniak KA, Gerlee P, Quaranta V. Microenvironment driven invasion: A multiscale multimodel investigation. *J Math Biol.* 2009. page 579–624.
83. Anderson ARA. A hybrid mathematical model of solid tumour invasion: the importance of cell adhesion. *Math Med Biol.* 2005;22:163–86.
84. Metzcar J, Wang Y, Heiland R, Macklin P. A Review of Cell-Based Computational Modeling in Cancer Biology. *JCO Clin Cancer Inform. American Society of Clinical Oncology (ASCO)*; 2019;1–13.
85. Ghaffarizadeh A, Heiland R, Friedman SH, Mumenthaler SM, Macklin P. PhysiCell: An open source physics-based cell simulator for 3-D multicellular systems. *PLoS Comput Biol. Public Library of Science*; 2018;14.
86. Hong CR, Bogle G, Wang J, Patel K, Pruijn FB, Wilson WR, et al. Bystander effects of hypoxia-activated prodrugs: Agent-based modeling using three dimensional cell cultures. *Front Pharmacol. Frontiers Media S.A.*; 2018;9:1013.
87. Li H, Torabi SJ, Yarbrough WG, Mehra S, Osborn HA, Judson B. Association of human papillomavirus status at head and neck carcinoma subsites with overall survival. *JAMA Otolaryngol Head Neck Surg* [Internet]. American Medical

- Association; 2018 [cited 2020 Nov 10];144:519–25. Available from: [/pmc/articles/PMC6583856/?report=abstract](https://pubmed.ncbi.nlm.nih.gov/33194713/)
88. Shen S, Yan Z, Wu J, Liu X, Guan G, Zou C, et al. Characterization of ROS Metabolic Equilibrium Reclassifies Pan-Cancer Samples and Guides Pathway Targeting Therapy. *Front Oncol* [Internet]. *Front Oncol*; 2020 [cited 2022 Feb 22];10. Available from: <https://pubmed.ncbi.nlm.nih.gov/33194713/>
 89. Son Y, Cheong Y-K, Kim N-H, Chung H-T, Kang DG, Pae H-O. Mitogen-Activated Protein Kinases and Reactive Oxygen Species: How Can ROS Activate MAPK Pathways? *J Signal Transduct*. Hindawi Publishing Corporation; 2011;2011.
 90. Best SA, de Souza DP, Kersbergen A, Policheni AN, Dayalan S, Tull D, et al. Synergy between the KEAP1/NRF2 and PI3K Pathways Drives Non-Small-Cell Lung Cancer with an Altered Immune Microenvironment. *Cell Metab*. Cell Press; 2018;27:935-943.e4.
 91. Koundouros N, Poulogiannis G. Phosphoinositide 3-Kinase/Akt Signaling and Redox Metabolism in Cancer. *Front Oncol*. Frontiers; 2018;0:160.
 92. Johansson K, Cebula M, Rengby O, Dreij K, Carlström KE, Sigmundsson K, et al. Cross Talk in HEK293 Cells between Nrf2, HIF, and NF-κB Activities upon Challenges with Redox Therapeutics Characterized with Single-Cell Resolution. *Antioxid Redox Signal*. Mary Ann Liebert Inc.; 2017. page 229–46.
 93. S M, S C, K V. Regulation of hypoxia-inducible factor-1a by reactive oxygen species: new developments in an old debate. *J Cell Biochem* [Internet]. *J Cell Biochem*; 2015 [cited 2021 Aug 26];116:696–703. Available from: <https://pubmed.ncbi.nlm.nih.gov/25546605/>
 94. Emanuele S, D'Anneo A, Calvaruso G, Cernigliaro C, Giuliano M, Lauricella M. The Double-Edged Sword Profile of Redox Signaling: Oxidative Events As Molecular Switches in the Balance between Cell Physiology and Cancer. *Chem Res*

- Toxicol [Internet]. American Chemical Society; 2018 [cited 2021 Aug 26];31:201–10. Available from: <https://pubs.acs.org/doi/abs/10.1021/acs.chemrestox.7b00311>
95. Badgley MA, Kremer DM, Maurer HC, DelGiorno KE, Lee H-J, Purohit V, et al. Cysteine depletion induces pancreatic tumor ferroptosis in mice. *Science* (1979) [Internet]. 2020;368:85–9. Available from: <https://www.sciencemag.org/lookup/doi/10.1126/science.aaw9872>
 96. Seibt TM, Proneth B, Conrad M. Role of GPX4 in ferroptosis and its pharmacological implication. *Free Radic Biol Med*. Elsevier Inc.; 2019. page 144–52.
 97. Adimora NJ, Jones DP, Kemp ML. A Model of Redox Kinetics Implicates the Thiol Proteome in Cellular Hydrogen Peroxide Responses. *Antioxid Redox Signal* [Internet]. 140 Huguenot Street, 3rd Floor New Rochelle, NY 10801 USA: Mary Ann Liebert, Inc.; 2010;13:731–43. Available from: <http://www.ncbi.nlm.nih.gov/pmc/articles/PMC2935341/>
 98. Cloer EW, Goldfarb D, Schrank TP, Weissman BE, Major MB. Nrf2 activation in cancer: From DNA to protein. *Cancer Res*. American Association for Cancer Research Inc.; 2019. page 889–98.
 99. Harris IS, DeNicola GM. The Complex Interplay between Antioxidants and ROS in Cancer. *Trends Cell Biol* [Internet]. 2020 [cited 2020 Apr 15]; Available from: <https://linkinghub.elsevier.com/retrieve/pii/S0962892420300581>
 100. Trachootham D, Alexandre J, Huang P. Targeting cancer cells by ROS-mediated mechanisms: A radical therapeutic approach? *Nat Rev Drug Discov*. 2009. page 579–91.
 101. Roh JL, Jang H, Kim EH, Shin D. Targeting of the Glutathione, Thioredoxin, and Nrf2 Antioxidant Systems in Head and Neck Cancer. *Antioxid Redox Signal*. Mary Ann Liebert Inc.; 2017;27:106–14.

102. Glorieux C, Calderon PB. Catalase, a remarkable enzyme: Targeting the oldest antioxidant enzyme to find a new cancer treatment approach. *Biol Chem*. Walter de Gruyter GmbH; 2017. page 1095–108.
103. AK J. Regulation of genes encoding NAD(P)H:quinone oxidoreductases. *Free Radic Biol Med* [Internet]. *Free Radic Biol Med*; 2000 [cited 2021 Sep 12];29:254–62. Available from: <https://pubmed.ncbi.nlm.nih.gov/11035254/>
104. Nioi P, McMahon M, Itoh K, Yamamoto M, Hayes JD. Identification of a novel Nrf2-regulated antioxidant response element (ARE) in the mouse NAD(P)H:quinone oxidoreductase 1 gene: reassessment of the ARE consensus sequence. *Biochemical Journal* [Internet]. Portland Press Ltd; 2003 [cited 2022 Nov 27];374:337. Available from: </pmc/articles/PMC1223621/?report=abstract>
105. Li LS, Reddy S, Lin ZH, Liu S, Park H, Chun SG, et al. NQO1-Mediated tumor-selective lethality and radiosensitization for head and neck cancer. *Mol Cancer Ther* [Internet]. American Association for Cancer Research Inc.; 2016 [cited 2020 Dec 7];15:1757–67. Available from: <https://pubmed.ncbi.nlm.nih.gov/27196777/>
106. Motea EA, Huang X, Singh N, Kilgore JA, Williams NS, Xie XJ, et al. NQO1-dependent, tumor-selective radiosensitization of non-small cell lung cancers. *Clinical Cancer Research*. American Association for Cancer Research Inc.; 2019;25:2601–9.
107. Puram S v, Tirosh I, Parikh AS, Patel AP, Yizhak K, Gillespie S, et al. Single-Cell Transcriptomic Analysis of Primary and Metastatic Tumor Ecosystems in Head and Neck Cancer. *Cell* [Internet]. 2017 [cited 2019 Oct 23];171:1611-1624.e24. Available from: <http://www.ncbi.nlm.nih.gov/pubmed/29198524>
108. Tirosh I, Izar B, Prakadan SM, Wadsworth MH, Treacy D, Trombetta JJ, et al. Dissecting the multicellular ecosystem of metastatic melanoma by single-cell RNA-seq. *Science* [Internet]. *Science*; 2016 [cited 2022 Mar 17];352:189–96. Available from: <https://pubmed.ncbi.nlm.nih.gov/27124452/>

109. Xiao Z, Dai Z, Locasale JW. Metabolic landscape of the tumor microenvironment at single cell resolution. *Nat Commun* [Internet]. Nature Publishing Group; 2019 [cited 2021 Apr 6];10:1–12. Available from: <https://doi.org/10.1038/s41467-019-11738-0>
110. Lewis JE, Forshaw TE, Boothman DA, Furdui CM, Kemp ML. Personalized Genome-Scale Metabolic Models Identify Targets of Redox Metabolism in Radiation-Resistant Tumors. *Cell Syst*. Cell Press; 2021;12:68-81.e11.
111. Oh G-S, Kim H-J, Choi J-H, Shen A, Choe S-K, Karna A, et al. Pharmacological activation of NQO1 increases NAD⁺ levels and attenuates cisplatin-mediated acute kidney injury in mice. *Kidney Int* [Internet]. 2013 [cited 2022 Nov 28];85:547–60. Available from: <http://www.kidney-international.org>
112. Lewis JE, Costantini F, Mims J, Chen X, Furdui CM, Boothman DA, et al. Genome-Scale Modeling of NADPH-Driven β -Lapachone Sensitization in Head and Neck Squamous Cell Carcinoma. *Antioxid Redox Signal* [Internet]. 2018 [cited 2020 Feb 4];29:937–52. Available from: <http://www.liebertpub.com/doi/10.1089/ars.2017.7048>
113. Hrovatin K, Fischer DS, Theis FJ. Toward modeling metabolic state from single-cell transcriptomics. *Mol Metab*. Elsevier; 2022;57:101396.
114. Schwanhäusser B, Busse D, Li N, Dittmar G, Schuchhardt J, Wolf J, et al. Global quantification of mammalian gene expression control. *Nature* 2011 473:7347 [Internet]. Nature Publishing Group; 2011 [cited 2021 Aug 15];473:337–42. Available from: <https://www.nature.com/articles/nature10098>
115. Zhao W, Jiang L, Fang T, Fang F, Liu Y, Zhao Y, et al. β -Lapachone Selectively Kills Hepatocellular Carcinoma Cells by Targeting NQO1 to Induce Extensive DNA Damage and PARP1 Hyperactivation. *Front Oncol*. Frontiers Media S.A.; 2021;11:4026.

116. Panieri E, Telkoparan-Akillilar P, Suzen S, Saso L. The NRF2/KEAP1 Axis in the Regulation of Tumor Metabolism: Mechanisms and Therapeutic Perspectives. *Biomolecules*. NLM (Medline); 2020.
117. Panieri E, Saso L. INHIBITION OF THE NRF2/KEAP1 AXIS: A PROMISING THERAPEUTIC STRATEGY TO ALTER REDOX BALANCE OF CANCER CELLS. *Antioxid Redox Signal* [Internet]. *Antioxid Redox Signal*; 2021 [cited 2021 Jan 10];ars.2020.8146. Available from: <https://www.liebertpub.com/doi/10.1089/ars.2020.8146>
118. Winski S, Koutalos Y, Bentley D, Ross D. Subcellular Localization of NAD(P)H:quinone Oxidoreductase 1 in Human Cancer Cells1 | *Cancer Research* | American Association for Cancer Research [Internet]. [cited 2022 Feb 22]. Available from: <https://aacrjournals.org/cancerres/article/62/5/1420/509711/Subcellular-Localization-of-NAD-P-H-quinone>
119. Ma J, Lim C, Sacher JR, van Houten B, Qian W, Wipf P. Mitochondrial targeted β -lapachone induces mitochondrial dysfunction and catastrophic vacuolization in cancer cells. *Bioorg Med Chem Lett* [Internet]. NIH Public Access; 2015 [cited 2022 Feb 22];25:4828. Available from: [/pmc/articles/PMC4607627/](https://pubmed.ncbi.nlm.nih.gov/254828/)
120. Thiagarajah JR, Chang J, Goettel JA, Verkman AS, Lencer WI. Aquaporin-3 mediates hydrogen peroxide-dependent responses to environmental stress in colonic epithelia. *Proc Natl Acad Sci U S A* [Internet]. National Academy of Sciences; 2017;114:568–73. Available from: [http://www.ncbi.nlm.nih.gov/pmc/articles/PMC5255594/](https://www.ncbi.nlm.nih.gov/pmc/articles/PMC5255594/)
121. Bienert GP, Chaumont F. Aquaporin-facilitated transmembrane diffusion of hydrogen peroxide. *Biochim Biophys Acta Gen Subj*. Elsevier; 2014. page 1596–604.

122. Bienert GP, Møller ALB, Kristiansen KA, Schulz A, Møller IM, Schjoerring JK, et al. Specific aquaporins facilitate the diffusion of hydrogen peroxide across membranes. *Journal of Biological Chemistry*. 2007;282:1183–92.
123. Watanabe S, Moniaga CS, Nielsen S, Hara-Chikuma M. Aquaporin-9 facilitates membrane transport of hydrogen peroxide in mammalian cells. *Biochem Biophys Res Commun* [Internet]. 2016 [cited 2019 Nov 13];471:191–7. Available from: <http://www.ncbi.nlm.nih.gov/pubmed/26837049>
124. Schwanhüsser B, Busse D, Li N, Dittmar G, Schuchhardt J, Wolf J, et al. Global quantification of mammalian gene expression control. *Nature* [Internet]. Nature Publishing Group; 2011 [cited 2020 Oct 27];473:337–42. Available from: <https://www.nature.com/articles/nature10098>
125. Xiao Z, Dai Z, Locasale JW. Metabolic landscape of the tumor microenvironment at single cell resolution. *Nature Communications* 2019 10:1 [Internet]. Nature Publishing Group; 2019 [cited 2022 Feb 22];10:1–12. Available from: <https://www.nature.com/articles/s41467-019-11738-0>
126. Lähnemann D, Köster J, Szczurek E, McCarthy DJ, Hicks SC, Robinson MD, et al. Eleven grand challenges in single-cell data science. *Genome Biology* 2020 21:1 [Internet]. BioMed Central; 2020 [cited 2022 Feb 22];21:1–35. Available from: <https://genomebiology.biomedcentral.com/articles/10.1186/s13059-020-1926-6>
127. Kim TH, Zhou X, Chen M. Demystifying “drop-outs” in single-cell UMI data. *Genome Biol* [Internet]. BioMed Central; 2020 [cited 2022 Feb 22];21:1–19. Available from: <https://genomebiology.biomedcentral.com/articles/10.1186/s13059-020-02096-y>
128. Qiu P. Embracing the dropouts in single-cell RNA-seq analysis. *Nature Communications* 2020 11:1 [Internet]. Nature Publishing Group; 2020 [cited 2022 Feb 22];11:1–9. Available from: <https://www.nature.com/articles/s41467-020-14976-9>

129. Bansal N, Mims J, Kuremsky JG, Olex AL, Zhao W, Yin L, et al. Broad phenotypic changes associated with gain of radiation resistance in head and neck squamous cell cancer. *Antioxid Redox Signal* [Internet]. *Antioxid Redox Signal*; 2014 [cited 2022 Apr 19];21:221–36. Available from: <https://pubmed.ncbi.nlm.nih.gov/24597745/>
130. Kippner LE, Finn NA, Shukla S, Kemp ML. Systemic remodeling of the redox regulatory network due to RNAi perturbations of glutaredoxin 1, thioredoxin 1, and glucose-6-phosphate dehydrogenase. *BMC Syst Biol* [Internet]. *BMC Syst Biol*; 2011 [cited 2022 Mar 16];5. Available from: <https://pubmed.ncbi.nlm.nih.gov/21995976/>
131. Moore CB, Guthrie EH, Huang MTH, Taxman DJ. Short Hairpin RNA (shRNA): Design, Delivery, and Assessment of Gene Knockdown. *Methods Mol Biol* [Internet]. NIH Public Access; 2010 [cited 2023 Mar 19];629:141. Available from: </pmc/articles/PMC3679364/>
132. Rao DD, Senzer N, Cleary MA, Nemunaitis J. Comparative assessment of siRNA and shRNA off target effects: what is slowing clinical development. *Cancer Gene Therapy* 2009 16:11 [Internet]. Nature Publishing Group; 2009 [cited 2023 Mar 19];16:807–9. Available from: <https://www.nature.com/articles/cgt200953>
133. Tsai KKC, Chuang EYY, Little JB, Yuan ZM. Cellular Mechanisms for Low-Dose Ionizing Radiation–Induced Perturbation of the Breast Tissue Microenvironment. *Cancer Res* [Internet]. American Association for Cancer Research; 2005 [cited 2023 Mar 6];65:6734–44. Available from: <https://aacrjournals.org/cancerres/article/65/15/6734/518419/Cellular-Mechanisms-for-Low-Dose-Ionizing>
134. Glicklis R, Merchuk JC, Cohen S. Modeling mass transfer in hepatocyte spheroids via cell viability, spheroid size, and hepatocellular functions. *Biotechnol Bioeng* [Internet]. John Wiley & Sons, Ltd; 2004 [cited 2023 Mar 6];86:672–80. Available from: <https://onlinelibrary.wiley.com/doi/full/10.1002/bit.20086>

135. Rangarajan A, Hong SJ, Gifford A, Weinberg RA. Species- and cell type-specific requirements for cellular transformation. *Cancer Cell*. Cell Press; 2004;6:171–83.
136. Céspedes MV, Casanova I, Parreño M, Mangués R. Mouse models in oncogenesis and cancer therapy. *Clinical and Translational Oncology* [Internet]. Springer; 2006 [cited 2023 Mar 6];8:318–29. Available from: <https://link.springer.com/article/10.1007/s12094-006-0177-7>
137. Raddatz AD, Furdui CM, Bey EA, Kemp ML. Single-Cell Kinetic Modeling of β -Lapachone Metabolism in Head and Neck Squamous Cell Carcinoma. *Antioxidants* [Internet]. MDPI AG; 2023 [cited 2023 Apr 25];12:741. Available from: <https://www.mdpi.com/2076-3921/12/3/741/htm>
138. Kipp AP, Deubel S, Arnér ESJ, Johansson K. Time- and cell-resolved dynamics of redox-sensitive Nrf2, HIF and NF- κ B activities in 3D spheroids enriched for cancer stem cells. *Redox Biol*. Elsevier B.V.; 2017;12:403–9.
139. Nikitina A, Huang D, Li L, Peterman N, Cleavenger SE, Fernández FM, et al. A Co-registration Pipeline for Multimodal MALDI and Confocal Imaging Analysis of Stem Cell Colonies. *J Am Soc Mass Spectrom* [Internet]. American Chemical Society; 2020 [cited 2023 Feb 26];31:986–9. Available from: </pmc/articles/PMC7370321/>
140. Nikitina AA, Grouw A Van, Roysam T, Huang D, Fernández FM, Kemp ML. Mass spectrometry imaging reveals early metabolic priming of cell lineage in differentiating human induced pluripotent stem cells. *bioRxiv* [Internet]. Cold Spring Harbor Laboratory; 2022 [cited 2023 Feb 26];2022.08.16.504020. Available from: <https://www.biorxiv.org/content/10.1101/2022.08.16.504020v1>
141. Al-Samir S, Itef F, Hegermann J, Gros G, Tsiavaliaris G, Endeward V. O₂ permeability of lipid bilayers is low, but increases with membrane cholesterol. *Cellular and Molecular Life Sciences* [Internet]. Springer Science and Business

- Media Deutschland GmbH; 2021 [cited 2023 Mar 5];78:7649–62. Available from: <https://link.springer.com/article/10.1007/s00018-021-03974-9>
142. Bienert GP, Schjoerring JK, Jahn TP. Membrane transport of hydrogen peroxide. *Biochim Biophys Acta Biomembr.* 2006. page 994–1003.
 143. Wang Z, Butner JD, Kerketta R, Cristini V, Deisboeck TS. Simulating Cancer Growth with Multiscale Agent-Based Modeling. *Semin Cancer Biol* [Internet]. 2015;0:70–8. Available from: <http://www.ncbi.nlm.nih.gov/pmc/articles/PMC4216775/>
 144. Olsen MM, Siegelmann HT. Multiscale Agent-based Model of Tumor Angiogenesis. *Procedia Comput Sci* [Internet]. 2013;18:1016–25. Available from: <http://www.sciencedirect.com/science/article/pii/S1877050913004109>
 145. Norton KA, Gong C, Jamalian S, Popel AS. Multiscale agent-based and hybrid modeling of the tumor immune microenvironment. *Processes.* MDPI AG; 2019;7.
 146. Cess CG, Finley SD, Mann AE. Fitting agent-based models to tumor images using representation learning. *bioRxiv* [Internet]. Cold Spring Harbor Laboratory; 2023 [cited 2023 Mar 7];2023.01.12.523847. Available from: <https://www.biorxiv.org/content/10.1101/2023.01.12.523847v1>
 147. Raddatz AD, Furdui C, Bey E, Kemp ML. Single cell kinetic modeling of redox-based drug metabolism in head and neck squamous cell carcinoma. *bioRxiv* [Internet]. Cold Spring Harbor Laboratory; 2022 [cited 2023 Mar 5];2022.05.17.492281. Available from: <https://www.biorxiv.org/content/10.1101/2022.05.17.492281v1>
 148. Rocha HL, Godet I, Kurtoglu F, Metzcar J, Konstantinopoulos K, Bhojar S, et al. A persistent invasive phenotype in post-hypoxic tumor cells is revealed by fate mapping and computational modeling. *iScience.* Elsevier; 2021;24:102935.
 149. Lewis JE, Kemp ML. Integration of machine learning and genome-scale metabolic modeling identifies multi-omics biomarkers for radiation resistance. *Nat Commun*

- [Internet]. Nature Publishing Group; 2021 [cited 2021 Aug 15];12. Available from: [/pmc/articles/PMC8113601/](#)
150. Quinlan CL, Treberg JR, Perevoshchikova I v., Orr AL, Brand MD. Native rates of superoxide production from multiple sites in isolated mitochondria measured using endogenous reporters. *Free Radic Biol Med*. Pergamon; 2012;53:1807–17.
 151. Muller FL, Liu Y, van Remmen H. Complex III releases superoxide to both sides of the inner mitochondrial membrane. *Journal of Biological Chemistry* [Internet]. Elsevier; 2004 [cited 2022 Nov 27];279:49064–73. Available from: <http://www.jbc.org/article/S0021925819322963/fulltext>
 152. Gonzalez H, Hagerling C, Werb Z. Roles of the immune system in cancer: from tumor initiation to metastatic progression. *Genes Dev* [Internet]. Cold Spring Harbor Laboratory Press; 2018 [cited 2022 Nov 27];32:1267. Available from: [/pmc/articles/PMC6169832/](#)
 153. Valkenburg KC, de Groot AE, Pienta KJ. Targeting the tumour stroma to improve cancer therapy. *Nat Rev Clin Oncol* [Internet]. NIH Public Access; 2018 [cited 2022 Nov 27];15:366. Available from: [/pmc/articles/PMC5960434/](#)
 154. Marx V. Method of the Year: spatially resolved transcriptomics. *Nature Methods* 2021 18:1 [Internet]. Nature Publishing Group; 2021 [cited 2022 Nov 27];18:9–14. Available from: <https://www.nature.com/articles/s41592-020-01033-y>
 155. Shen Y, Li S, Wang X, Wang M, Tian Q, Yang J, et al. Tumor vasculature remodeling by thalidomide increases delivery and efficacy of cisplatin. *J Exp Clin Cancer Res* [Internet]. 2019 [cited 2019 Oct 28];38:427. Available from: <http://www.ncbi.nlm.nih.gov/pubmed/31656203>